Materials & Design 250 (2025) 113615

Contents lists available at ScienceDirect

Materials & Design

journal homepage: www.elsevier.com/locate/matdes

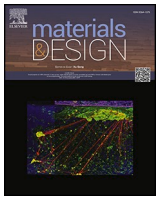

Modelling and measurements of thermally induced residual stress in IN718 nickel-based superalloy during non-uniform quenching

S. Rahimi [a,*], M. King [a], M. Amir Siddiq [b], B.P. Wynne [a,c]

[a] Advanced Forming Research Centre (AFRC), University of Strathclyde, 85 Inchinnan Drive, Inchinnan, Renfrewshire, PA4 9LJ, UK
[b] School of Engineering, University of Aberdeen, Aberdeen, AB24 3UE, UK
[c] Department of Mechanical and Aerospace Engineering, University of Strathclyde, James Weir Building, 75 Montrose Street, Glasgow, G1 1XJ, UK

ARTICLE INFO

Keywords:
Residual stress
Nickel-based superalloys
Contour method
Heat transfer coefficient (HTC)
Incremental central hole-drilling (ICHD)
Quenching

ABSTRACT

Residual stress induced during and as a result of manufacturing processes can have a significant impact on the later stages of manufacturing (e.g., machining), and in-service performance (e.g., resistance to fatigue) of a component. In this work, a novel approach is presented by combining FE based residual stress predictions with experimental verification at scales comparable to industrial components, which is rarely reported. Instrumented plates of IN718 nickel-based superalloys have been water-quenched and air-cooled from solution annealing temperature (980 °C) and the associated cooling curves were measured at specified locations. The cooling curves were used as boundary conditions for inverse calculation of zone-specific heat transfer coefficient (HTC), which is the main parameter to estimate the heat exchange rate between different regions of a heated part and its surrounding environment. The HTCs have then been implemented in an elastic–plastic finite-element model, which included temperature dependant thermo-mechanical properties to predict thermally induced residual stress fields during heterogeneous water/air quenching from. For the verification of the model, identical plates were heterogeneously quenched (half in water and half in air) from 980 °C, both vertically and horizontally, and residual stress was then measured in both plates using the contour method and incremental central hole drilling.

1. Introduction

Nickel-based superalloys are attractive materials for use in demanding environment applications owing to their excellent combination of high temperature mechanical properties, good weldability and corrosion resistance. For example, they are extensively used in critical rotating parts for jet turbine engines and electricity generation systems where high temperature fatigue and creep resistance is essential for maintaining structural integrity.

One of the most widely used nickel-based superalloys is the precipitation strengthened alloy IN718 that has robust thermo-mechanical properties up to temperatures of 650 ℃ [1]. The high temperature mechanical strength of the alloy is derived from the precipitation of finely dispersed Ni_3Nb (γ') and Ni_3(Al, Ti) (γ') particles in the face-centred cubic (fcc) matrix of the Ni [1,2]. The disc-shaped body-centred tetragonal γ'' particles have a diameter in the region of 50 nm (or less) and a thickness in the region of 10 nm precipitate between 620 ℃-900 ℃, and because of the coherency strains between the c-axis of the γ'' and the matrix is the major strengthening mechanism [5]. The coherent fcc γ' particles further contribute to strength owing to moving dislocations having to overcome the atomic order of the precipitates [6]. Above 650 ℃ IN718 loses strength because the Ni_3Nb precipitates as the more stable orthorhombic δ-phase (≈700 ℃ − 1000 ℃) that nucleates at grain boundaries and grows as thin plates on the {111} crystallographic planes of the face-centred cubic (fcc) matrix, extending into the grains [1,3]. There is minimal strengthening effect of δ-phase but its presence is beneficial for grain boundary pinning to prevent grain growth during solution heat treatments [4], and to improve resistance to grain boundary creep fracture during service [5,6]. Furthermore, carbides also precipitate through the addition of carbon, while increased mechanical resistance is achieved through solid solution hardening owing to the addition of molybdenum [7]. The presence of a notable amount of iron results in lower price, compared to other nickel-based superalloys with higher fraction of rare alloying elements like cobalt, such that the alloy is often referred to as a nickel–iron alloy.

To acquire the desirable mechanical properties for the aforementioned critical applications, the microstructure, including the size and distributions of grain sizes and different precipitates, needs to be

* Corresponding author.
E-mail address: salah.rahimi@strath.ac.uk (S. Rahimi).

https://doi.org/10.1016/j.matdes.2025.113615
Received 17 September 2024; Received in revised form 13 January 2025; Accepted 13 January 2025
Available online 15 January 2025
0264-1275/© 2025 The Authors. Published by Elsevier Ltd. This is an open access article under the CC BY license (http://creativecommons.org/licenses/by/4.0/).

designed and controlled during manufacturing processes [1,8–10]. For this purpose, the material is typically subjected to sequential thermo-mechanical processing comprising of solution heat treatment at temperatures close to the solvus temperature of δ-phase (i.e., slightly above or below) followed by rapid cooling (e.g., water-quenching), and subsequent heat treatments at lower temperatures (i.e., 720 ℃ and 620 ℃) [1,11]. The aging heat treatments at 720 ℃ and 620 ℃ leads to the precipitation of γ″ and γ′ intragranularly, which are critical for high temperature mechanical properties and creep resistance [12,13].

The thermal gradients experienced by a part during post-forging water-quenching from the solution heat treatment temperatures can generate a residual stress field of significantly high magnitude [14–16]. The aging heat treatments at lower temperatures (i.e. 575 ℃ − 720 ℃), after solution treatments, might relieve this stress, however it is rare for the stress field to be completely relaxed [11]. This stress field is generated during quenching because of the differential expansion and contraction between the cold exterior and the heated interior of the part, causing extreme misfit between the two regions that eventually results in heterogeneous plastic deformation [17,18]. The rate at which heat is extracted from a component determines the severity of the differential gradient in temperature and therefore affects the magnitudes and distribution of the resulting residual stress. Quantitative characterisation of convective heat transfer between the surface of a heated part and the surrounding medium (e.g., water), requires a good estimate of the heat transfer coefficient (HTC), as the main parameter in the Newton-Richmann relation [19]. The HTC is dependent on both the physical properties of the quenchant and the physical situation of the quenching process [20]. It is an empirically determined parameter whose value is a function of the variables affecting convention such as the part's surface properties (e.g., geometry and roughness), the properties of the quenchant, fluid dynamic, and the nature of the quenchant motions [21].

The generated residual stress field remains in the part in the absence of external loading, and can be beneficial or detrimental to the performance of the material in critical environments [18]. Compressive residual stress is known to benefit fatigue performance [22], for instance the stress generated at the surface of a component through shot peening [23]. Conversely, tensile residual stress decreases the resistance of the material to different degradation mechanisms and can lead to premature failures [24]. Additionally, and most importantly, they can influence the strategies based on which the final machining operations of the manufacturing processes are executed. This is primarily due to the redistribution of residual stress caused by material removal which results in distortion of the remaining material out of required dimensional tolerances. Therefore, accurate prediction of the generation and evolution of residual stress during manufacturing processes are essential for component design and right-first-time manufacture.

Inverse heat transfer analysis method has commonly been used for the estimation of HTC by applying the cooling curves, measured during quenching, as boundary conditions [25–31]. Despite the practicality of this approach, it often requires large number of data points, especially for complex geometries, to provide a reasonable estimate of localised HTCs. This method has been adopted in this study aiming to present a clear understanding of the magnitude and distribution of thermally induced residual stress generated during heterogeneous cooling of IN718 from solution annealing temperature (980 ℃). The effect of quenching configuration and extreme temperature gradient on residual stress distribution are investigated by both finite element (FE) modelling and experimental measurements. The implemented methodology provides a mean of comparison between the results of FE modelling and those of the residual stress measurement techniques. Previous studies investigating quenching induced residual stress in IN718 exist in literature (e.g., [17,32–34]), however the combination of modelling of residual stress based on HTCs calculated using the inverse analyses method and comparison with the results of measurements using a relevant technique (e.g., contour method) at scales comparable to industrial parts can rarely be found. Therefore, the procedure presented in this paper can provide manufacturers with an approach to estimate quenching induced residual stress to better control its effects during later stages of manufacturing, e.g., abiding by the required dimensional tolerances during machining.

2. Experimental procedures

This section introduces the material, and describes the methodologies used for acquiring the necessary data for further analyses and FE prediction of the effect of heterogeneous cooling and quenching configuration on the generation and distribution of residual stress. Initially, the material is introduced, and details of microstructural characterisations on the as-received and heat-treated conditions are described. Then the experimental methodologies are divided into two folds, (i) measurements of cooling curves at specified locations of the plate geometry during water quenching (i.e., in both vertical and horizontal configurations), and (ii) measurements of residual stress using incremental central hole-drilling (ICHD) and contour method. The measured cooling curves are then used as input for FE simulations which are described in later sections, and the results of residual stress measurements are used for validation and verification of the results of predictive models which are explained in the discussion section.

2.1. Material and microstructure

The material used for this study was IN718 supplied by Aubert & Duval in billet form with 300 mm diameter and 2500 mm length. The chemical composition, supplied by the manufacturer, is provided in Table 1. Four flat plates with 250 mm × 200 mm × 30 mm (L × W × T) dimensions were machined from the as-received billet to a Ra ≈ 3 μm surface finish. Two plates were used for the measurement of cooling curves during quenching (one vertical and one horizontal quench), and the remaining two plates were used for residual stress measurements (one partial vertical and one partial horizontal water quench). A small cubic sample was also cut from the billet for microstructure characterisation of the as-received material.

Scanning electron microscope (SEM) and electron backscatter diffraction (EBSD) were used for microstructure characterisation in the as-received condition, and after solution annealing heat treatment for both the water quenched and air-cooled sections. The samples were ground and polished to a mirror finish condition followed by a 3 h vibratory polishing using colloidal silica suspension. EBSD was conducted using an automated HKL-EBSD system interfaced to a FEI Quanta-250 SEM, with an accelerating voltage of 20 kV and a 100 μm dia. aperture. A typical scan area size of 600 μm × 500 μm was acquired for each case, with over 90 % of the points indexed.

2.2. Quenching and measurements of cooling curves

For the measurements of temperature evolution during quenching, thermocouple holes with ≈1.1 mm diameter were drilled at specified locations using an electrical discharge machine (EDM). Fig. 1 schematically shows the positions of the thermocouples' tips for both vertical and horizontal quenching configurations. N-type thermocouples with 1 mm diameter and 2 m length were installed at each location. The thermocouples were secured using a high temperature cement to prevent any potential movement during quenching. The plates were then placed in a furnace and heated to 980 ℃ and kept at this temperature for an hour, once all areas of the plate had reached the target temperature. The plates were then removed via a forklift and quenched in water. For the vertical and horizontal quenching configurations, the width and thickness of the plates were aligned with the quenching direction, respectively. For sample handling with the forklift, specially designed holders were attached to the plates using M16 bolts, and an extension fork was manufactured and installed on the forklift such that the plates, with all the attached thermocouples, were safely removed from the

Table 1
Chemical composition of the IN718 material investigated in this study (wt%).

(wt%)	Ni	Cr	Fe	Mo	Nb + Ta	Al	Mn	C	Ti	P	Co	S	B	Cu	Si
Min.	50	17.0	Bal.	2.800	4.75	0.200	–	–	0.650	–	–	–	–	–	–
Max.	55	21.0		3.300	5.50	0.800	0.350	0.080	1.150	0.015	1.000	0.015	0.006	0.300	0.350

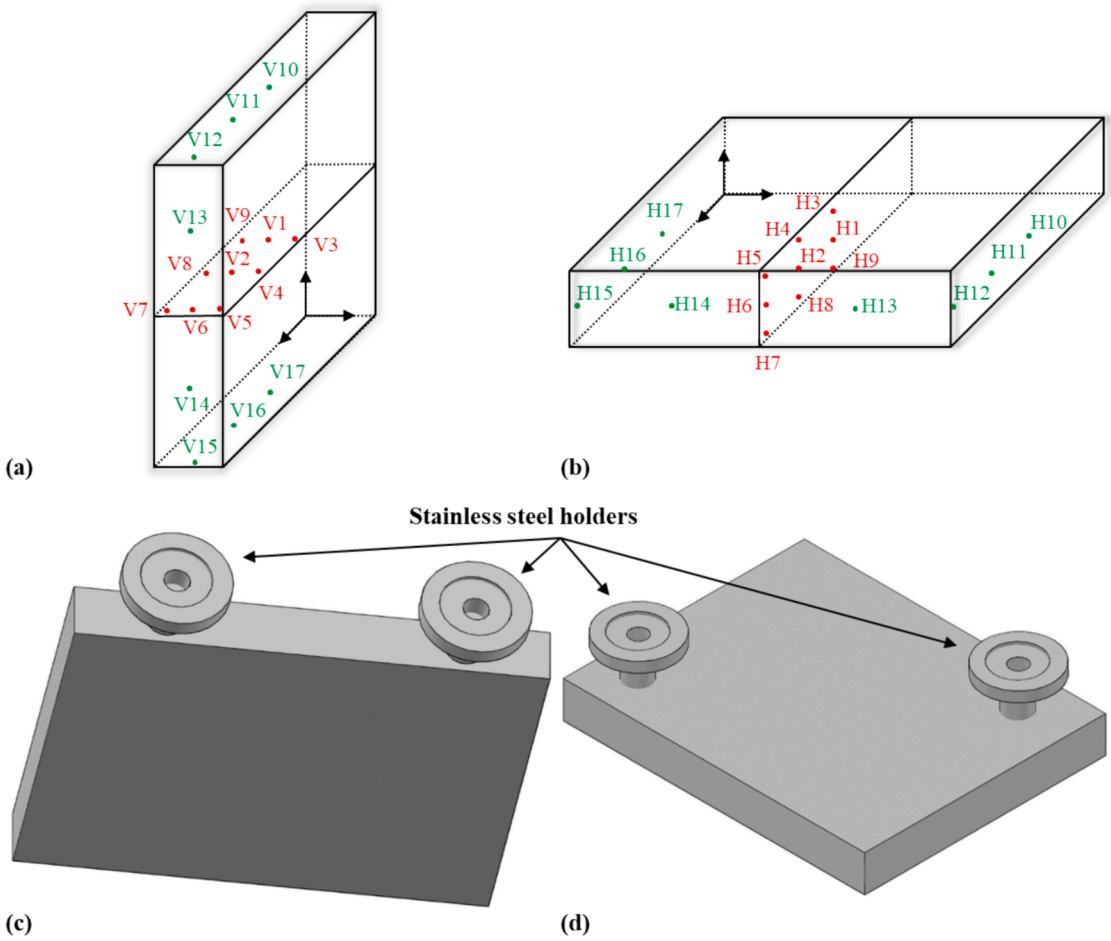

Fig. 1. Schematic sketches of the positions of the thermocouples instrumented into the plates during (a) vertical, and (b) horizontal quenching. (c) and (d) are the CAD models of the vertically and horizontally quenched plates, respectively, with the stainless-steel holders attached via M16 bolts for manual handling during quenching.

furnace and transferred to the quench tank in ≈ 14 s. During quenching, the samples were suspended from the fork such that their entire surfaces were in contact with water (see Fig. 1). Following water-quenching trials, the plates were returned to the furnace and solution heat treated at 980 ℃ for 1 h. The heated plates were then air cooled to the room temperature (≈20 ℃) and the cooling rates were monitored at different locations, similarly to the water-quenching experiments. The thermocouples were connected to National Instrument (NI) analogue temperature-input modules (i.e., installed on a NI 4-slot chassis) and controlled by LabView Signal Express software. The temperature at each thermocouple tip was measured at 10 Hz for the water-quenching trials, and at 1 Hz for the air cooling.

The remaining two plates for residual stress measurements were heated to 980 ℃, in the same furnace and under the same conditions as those for the measurements of cooling curves, and manually quenched in water one vertically half-way through its width, and the other horizontally half-way through its thickness (see Fig. 2). The manual quenching was carried out in less than 5 s transfer time from the furnace into the quench tank using a pair of high temperature resistance chain gloves without then requirement for other handling tools such as tongs. This method of quenching (i.e., half in water and half in air) was conducted to deliberately introduce extreme differential expansions and contractions into the parts during quenching, to investigate the effect of sample configuration on the distribution of thermally induced residual stress. This has then been used for the validation of the results of FE prediction.

2.3. Residual stress measurements

Measurements of residual stress were carried out on both plates in the as-quenched condition, following non-uniform vertical and horizonal quenching. The measurements were conducted by the aid of two different techniques: semi-destructive incremental central hole-drilling (ICHD) and the contour method.

2.3.1. ICHD method

Measurements by ICHD was conducted using a MTS3000-Restan hole-drilling apparatus manufactured by SINT Technology. For each measurement point, the target surface of the as-quenched plates was ground successively by 200 and 400 grit emery paper around the

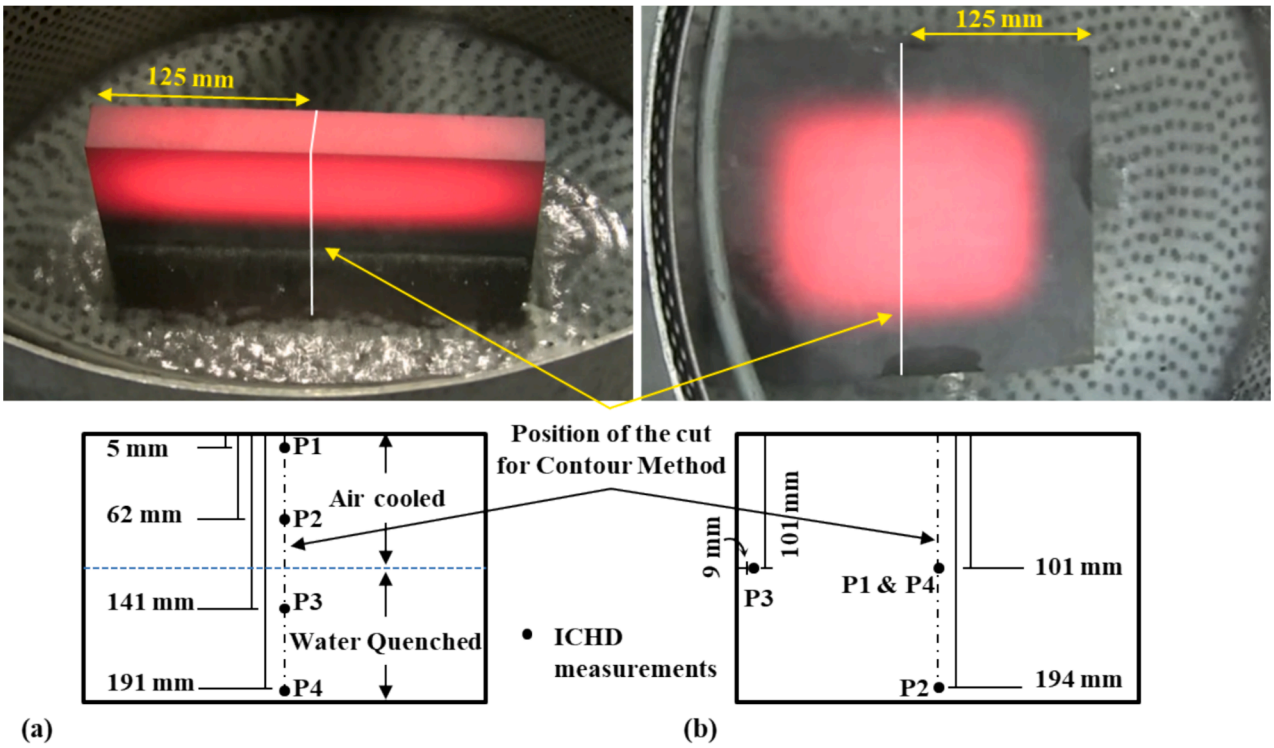

Fig. 2. Photographs of the heterogeneously cooled plates taken half way through the cooling process during manual quenching (i.e., half in water and half in air), with the schematic representations of the locations of the residual stress measurements with contour method and ICHD, (a) vertically quenched plate, and (b) horizontally quenched plate. Note that in (b) only one side of the plate (i.e., the air-cooled side) is illustrated where position P1 of the ICHD is on the air-cooled side and position P4 is on the opposite side of P1 (i.e., on the water-quenched side).

measurement area, removing up to about ~ 100 μm, including the oxide scale formed during heat treatment and quenching, for strain gauge installation. Following surface preparation and cleaning, pre-wired type 1-RY61-1.5/120R quarter bridge strain gauge rosettes, manufactured by HBM, were fitted at specified locations on both plates. For drilling holes at each point, 1.8 mm dia. TiAlN coated endmill, supplied by SINT Technology, was used. The measurements were carried out in compliance with the ASTM E837 standard [35] for uniform and non-uniform stress distributions. By implementing a suitable acquisition strategy, i.e., fine steps close to the surface and larger steps afterward, the holes were drilled up to 60 % of the drill diameters (~ 1.2 mm). The principal stresses were then calculated by taking into consideration the strains measured throughout the hole-drilling process according to the ASTM standard. Material's elastic properties including Young's Modulus of 196,000 MPa and Poisson's ratio of 0.294 were implemented, which were the same as those used for the contour method.

The measurements were carried out at four locations for each case, mainly on a surface trajectory bisecting the as-quenched plates symmetrically along the quenching directions such that the areas of the samples subjected to both air-cooling and water-quenching were examined. Fig. 2 schematically shows the locations of the residual stress measurements. The uncertainties of the measurements were analysed using an in-house developed software in MATLAB, using the compliance coefficients provided in ASTM E837 standard [35].

2.3.2. *Contour method*

Following the ICHD stress measurements the plates were subjected to the contour method of residual stress measurement to evaluate full 2D distribution of residual stress using displacement measurements normal to a cut plane matching the surface trajectory used for the ICHD measurement points, Fig. 2. The procedure for each sample comprised of four consecutive steps: (i) cutting, (ii) measurement of 2D surface displacement profiles of each half of the cut plate, (iii) surface displacement data processing, and (iv) inverse calculation of residual stress by FE simulation using the measured surface displacement contours as boundary conditions. The cutting was conducted by an EDM using a 250 μm brass wire in 'skim' cut mode. For each case, the sample was clamped as close as possible to the cut line on both sides of the cut plane to prevent potential solid body movements during the cut, which can add artefacts to the measurements [36]. Before the cut, two pilot holes with 1 mm diameter, were drilled at both ends of the cut plane 2 mm from each edge. The cut was then carried out from the centre of a hole on one side to the centre of the hole on the other side, aiming to make the part self-constraining preventing opening and closing of the cut faces, thereby avoiding stress concentration and the risk of significant plastic deformation arising at the cut tip during cutting. Upon the completion of the cut, the remaining ligaments on both sides were cut by the EDM to separate both halves of the parts.

Following the completion of the cuts by EDM, the outlines and the surface topographies of both half-cuts for each plate were measured using a Mitutoyo Crysta Apex C coordinate measuring machine (CMM) with a 2 mm ruby interfaced to a Renishaw PH10T touch probe, in an environmentally controlled lab. The data were acquired with a spatial resolution of 500 μm in both in-plane directions.

The obtained data clouds were cleaned by eliminating outliers and system noises, to minimise potential artefacts during the final residual stress simulation. The cleaned data from both half cuts of each plate were aligned in the same coordinate system, by mirroring one side of the cut on the other, and linearly interpolating them onto a common grid, where the two data clouds were averaged. The pitch size of the common grid was equal to that of the initial data to make sure that the averaged data points match those of the original data. A set of knots, with intervals ranging from 0.5 mm to 16 mm was selected and a bivariate cubic spline for each knot spacing was fitted to the averaged data. These were used as boundary conditions in the FE analysis for the evaluation of residual stress.

Three-dimensional (3D) FE models of the plates were constructed in the commercial FE software ABAQUS, assuming isotropic elasticity, a Young's modulus of 197,000 MPa, a Poisson's ratio of 0.294, and taking the averaged surface contour data (i.e., the bivariate cubic spline fits) as boundary conditions. For the construction of the 3D models, the measured perimeter of the cut cross-section for each case, after alignment in the same coordinate system as the data cloud, was extruded to 250 mm. A mesh was then generated using seeds as a guideline attributed to each node on the perimeter of the cut cross-section as well as along the direction of the extrusion. The density of seed attribution was biased along the extrusion direction to generate a finer mesh near the surface representing the cut and a coarser mesh towards the other end of the model that is not of interest for these calculations. The element spacing on the cut surface was 0.5 mm, equivalent to the initial CMM data acquisition pitch size, and 0.5 – 10 mm with single bias away from the cut surface. The element type used for these simulations was C3D20R with 20 nodes brick quadratic elements, as used in previous works [37,38]. The residual stress was then simulated, based on Bueckner's superposition principal, by forcing the representative cut surface to match the averaged surface contour data reversed in the out-of-plane direction (assuming that all deformations occurred elastically) [39–42].

3. Results

This section presents the results of microstructure analysis of the as-received and heat treated materials, which is then followed by the results of cooling curves recorded during quenching, and finally the results of residual stress measurements by the aid of different methods (i.e., ICHD and the contour method). These experimental results are then used in the following sections for the validation and comparison with the results of FE model predictions.

3.1. Microstructure

Fig. 3a and b show orientation image maps obtained by EBSD for the as-received and the heat-treated and water quenched microstructures using inverse pole figure (IPF) colouring with respect to the out-of-plane direction. Fig. 3c and d show the equivalent SEM images of Fig. 3a and b, respectively. It should be noted the EBSD and SEM images of the heat-treated and air-cooled microstructures look almost the same as those presented in Fig. 3b and d. This is because the cooling rate predominantly affects the size and distribution of γ'' [1,11], with only a small effect on grain size and δ-phase (i.e., white features), which cannot be resolved by SEM. Both microstructures appear to have random texture with no dominant preferred orientation. The as-received material had a microstructure with equiaxed grains of 3.0 ± 0.2 μm average grain size.

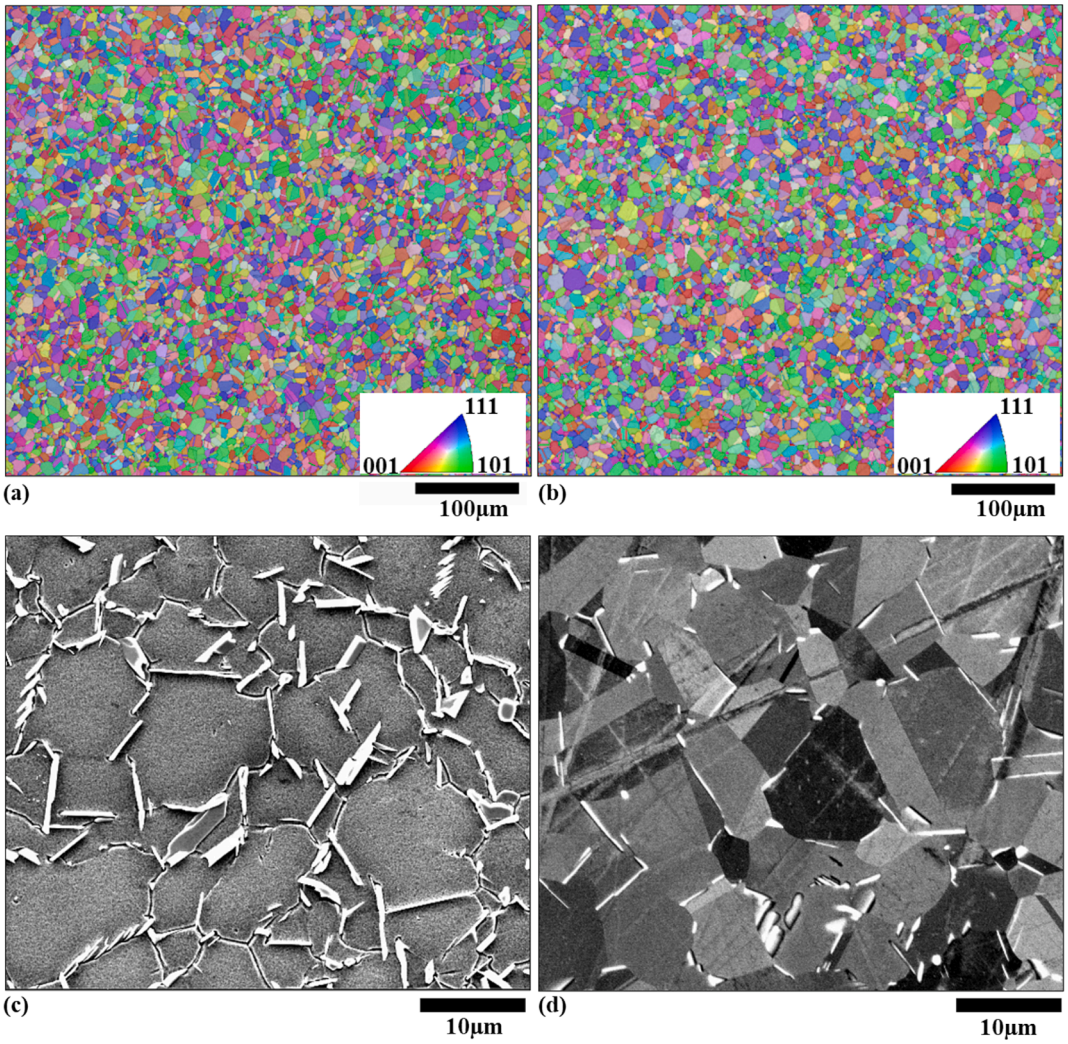

Fig. 3. (a) and (b) are the EBSD IPF colouring orientation maps with respect to the out-of-plane direction of the as-received, and heat-treated (1 h at 980 °C) and water-quenched materials, respectively, (c) and (d) are their corresponding SEM micrographs, respectively. δ-phase in (c) and (d) appear as white features lying on grain boundaries.

The 1 h solution heat treatment at 980 ℃ has led to the dissolution and dwindling of δ-phase by approximately 3–5 % volume fraction, evaluated from the SEM micrographs (see Fig. 3c, d), and a small grain growth by ~ 1 μm, so that the average grain size of the heat-treated microstructure became 3.9 ± 0.3 μm. Fig. 3c and d show higher magnifications backscattered electron (BSE) SEM micrographs of the as-received and the heat-treated microstructures illustrating δ-phase as white features at grain boundaries. The morphology of δ-phase changes depending on the heat treatment temperature such that it tends to become spheroidal over 985 °C and plate-like below 930 °C. The results of previous reports showed that solution treatments between 950 °C – 985 °C (i.e., between these two extreme temperatures) led to a mixture of both spheroidal and plate-like δ-phase [11,43,44], similarly to the observations made in this study (see Fig. 3c, d). Although the heat treatment at 980 °C has reduced the volume fraction of δ-phase by becoming thinner and more spherodised, however, their number fraction remained largely unchanged and hence as effective as the as-received material for grain boundary pinning (i.e., similar grain size).

3.2. Experimental cooling curves

The recorded cooling curves at various locations of the plates are shown in Fig. 4 and Fig. 5, respectively for the vertically and horizontally quenched plates. For both quenching configurations, the time at which the furnace door was opened and the time when the sample was picked-up from the furnace, transferred and fully immersed in water in the quench tank can be distinguished from the cooling curves, especially those installed at the corners of the plates. These are highlighted in Fig. 4b for the vertically quenched plate, and it looks very similar for the horizonal configuration as well (Fig. 5). The entire process from the opening of the furnace door to the full immersion in the tank takes about 24 s, with ~ 12 s transfer time (see Fig. 4b). Following the immersion of the samples, there are three distinct cooling mechanisms occurring during quenching that can be identified from the cooling curves. Initially, vapour-blanket forms around the plates; this is driven by the thermal gradient between the surface of the components and water, leading to the creation of Leidenfrost effect [45]. This stage can clearly be seen during vertical quenching for V3, V4, V8 and V9 (see Fig. 4b), and during horizonal quenching for H3, H4, H8 and H9 thermocouples

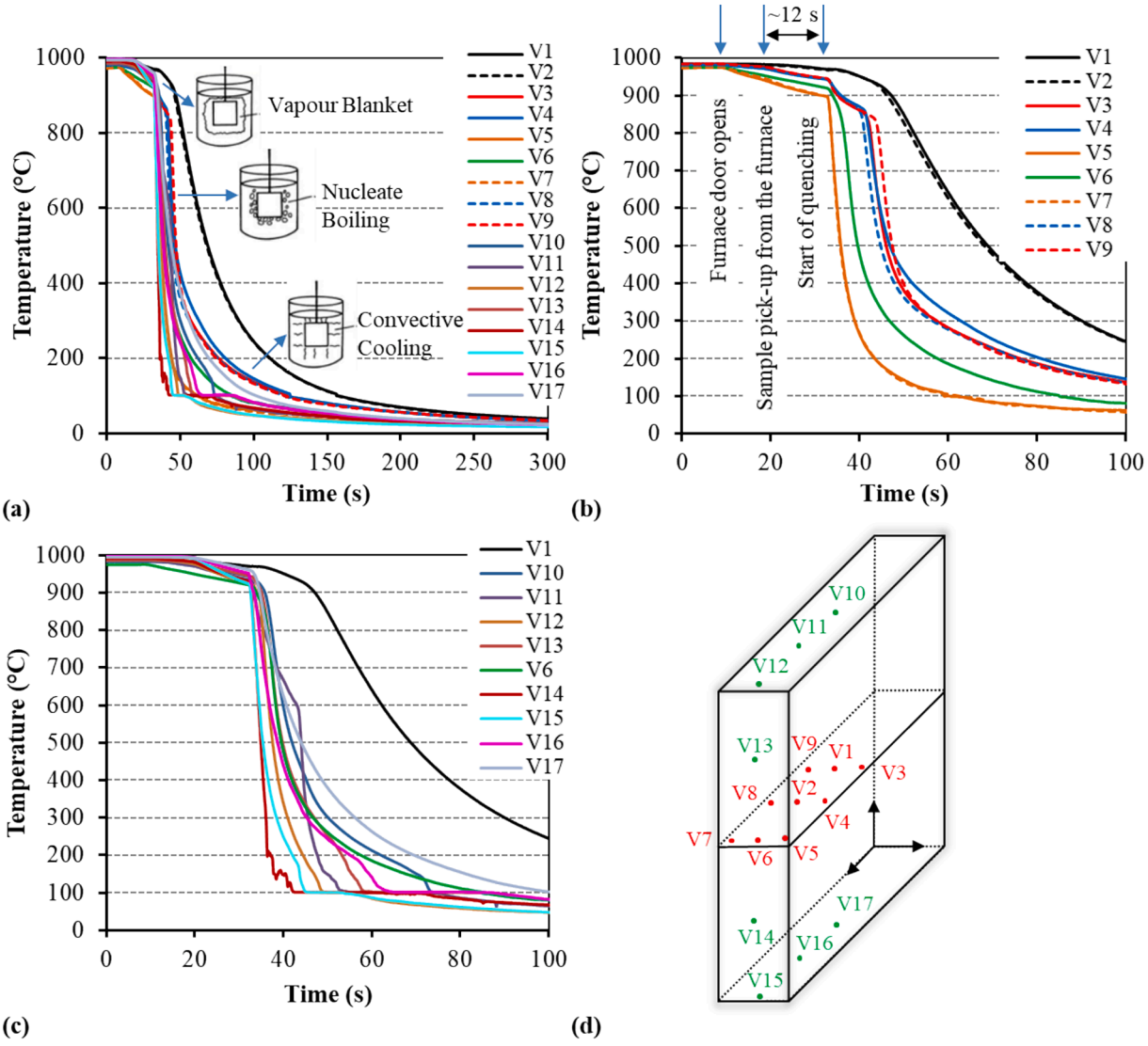

Fig. 4. Plots of cooling curves recorded during vertical water-quenching of an IN718 plate from 980 °C, (a) results of all thermocouples, (b) results of the thermocouples installed on a cross-sectional plane at mid-width (i.e., V1-V9 shown in (d)), (c) results of those installed on a through thickness cross-section (i.e., V6, V10 – V17 shown in (d)) from the beginning to 100 s into the quenching, and (d) schematic illustration of the vertically quenched plate and the locations of all thermocouples.

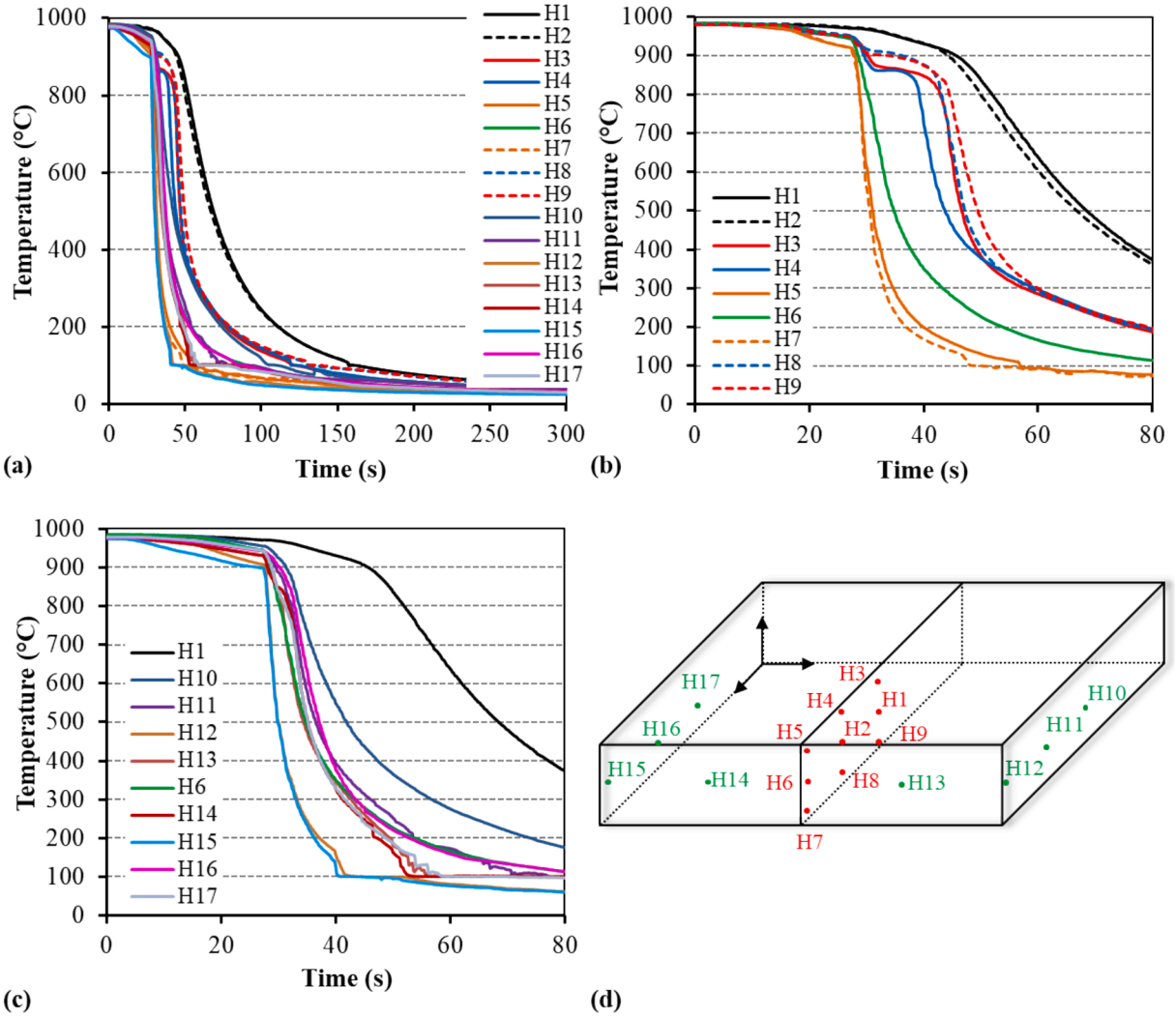

Fig. 5. Plots of cooling curves recorded during horizontal water-quenching of an IN718 plate from 980 °C, (a) results of all thermocouples, (b) results of the thermocouples installed on a cross-sectional plane at mid-width (i.e., H1-H9 shown in (d)) from the beginning to 80 s of quenching, (c) results of those installed on a through thickness cross-section (i.e., H6, *H*10 – H17 shown in (d)) up to 80 s of quenching, and (d) schematic illustration of the horizontally quenched plate and the locations of all thermocouples.

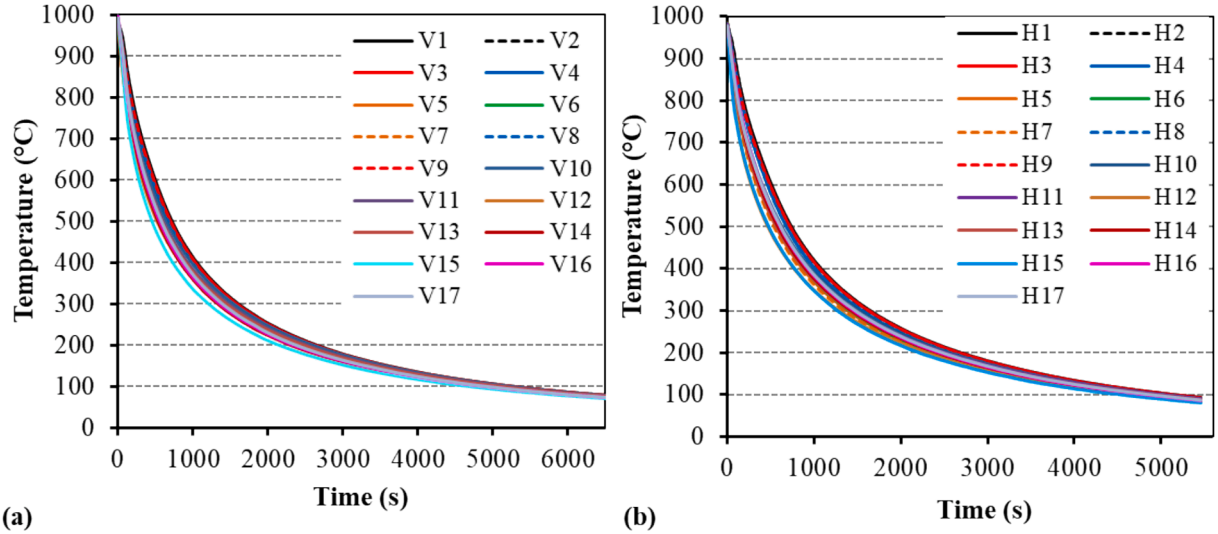

Fig. 6. Plots of cooling curves recorded during air cooling of the plates from 980 °C that were (a) vertically and (b) horizontally water-quenched previously. Note that the positions of thermocouples are identical to the water-quenching experiments (see Fig. 4 and Fig. 5 for the results).

(see Fig. 5b). As the components cool further, the insulating vapour jacket starts to break up and vapour-transport cooling (i.e., nucleate boiling) takes over, increasing the cooling rate as water contacts the surface. Finally, the component temperature drops below the water boiling point and quenching enters a liquid cooling phase. These stages are highlighted schematically in Fig. 4a for the vertical quenching configuration and more details about these stages can be found elsewhere [20].

The component geometry and its configuration during quenching affect the evolution of cooling behaviour. Vapour entrapment in cavities, for example, can leave areas insulated, relative to neighbouring regions, transitioning into a vapour-transport regime. The creation and subsequent breakup of the vapour layer has a strong effect on thermal gradients and subsequent material properties.

Fig. 6 shows the recorded cooling curves during air-cooling for the vertically and horizontally quenched plates, at the same spots as those for water-quenching trials. Unlike water-quenching, the cooling curves throughout the plates appear to be almost the same, implying that the rather slower heat exchange rate with the surrounding environment (i.e., air) is controlling the cooling. The sample configuration in this case has a minimum effect on cooling as the results of both plates appear to be similar. It has taken more than 5000 s for the temperature at the centre of the plates to reach temperatures below 100 °C in both cases, whereas during water-quenching the same spots reached room temperature in less than 300 s.

3.3. Residual stress measurements

Fig. 7a and b show the 3D surface profiles (i.e., data clouds) measured by CMM using hen-pick method (i.e., point by point) on the cut surfaces (i.e., one half-cut each) of the vertically and horizontally quenched samples, respectively. The full dataset, including the outlying data points affected by the edges and EDM-wire breakage are also provided to show the cleanness of the acquired surface profiles. Fig. 7c and d show their corresponding contour plots of the surface height, averaged from the data measured from the surfaces of both half-cuts, for each plate. The range of peak to valley of the contours exceeds ≈ 220 μm for the vertically quenched plate and ≈ 390 μm for the horizontally quenched plate. The contour plot for the former shows a wavy distribution of the surface data with a valley in the air-cooled half and a peak in the water-quenched side, while the contour plot of the latter shows a single valley with a shape like a wide upside-down bell. The areas with negative average surface height are affected by tensile residual stress, and vice versa, those with positive average height are affected by compressive.

The contour plots of the out-of-plane residual stress for both vertically and horizontally quenched plates are shown in Fig. 8a and b, respectively. These plots illustrate completely different residual stress patterns for the plates, depending on the direction of water-quenching (i.e., quenching configuration), while the maximum and minimum of the generated stress are comparable. For the vertically quenched plate (Fig. 8a) a significantly large tensile residual stress field developed in the mid air-cooled section, counterbalanced by compressive stress on top of the plate (i.e., far left). In the water-quenched side of the vertically quenched plate, the stress is rather uniformly distributed over the plate's cross-section with the middle region containing tensile stress surrounded by compressive stress in the outer regions. Though a distinct zone can be seen in the interference between air-cooled and water-quenched sections where almost no stress exists in the centre with similar compressive stress fields on both sides. Overall, the stress distribution in the vertically quenched plate appears to be symmetrical with respect to the width axis, which is expected due to the sample symmetry and the fact that both sides of the plate undergo similar conditions during quenching.

For the horizontally quenched plate (Fig. 8b), tensile residual stress field was measured in the centre of cross-section along the width, counterbalanced by compressive stress on both sides of the plate. The stress field is not symmetrical with respect to the width axis and appears to be shifted towards the water-quenched side. This matches the result of visual observation inspection made on this plate where the water-quenched side was concaved and the air-cooled side was convex following quenching, compared to straight plate in the as-received condition.

Fig. 9 shows the results of ICHD residual stress measurements carried out on both vertically and horizontally quenched plates, in both longitudinal and transverse directions. The measured near surface stress components indicate different stress magnitudes and profiles depending on the position of the measurements in the plates. These stress profiles are compared with the results of contour method and the relevant predicted stress by FE simulations and presented later in the discussion.

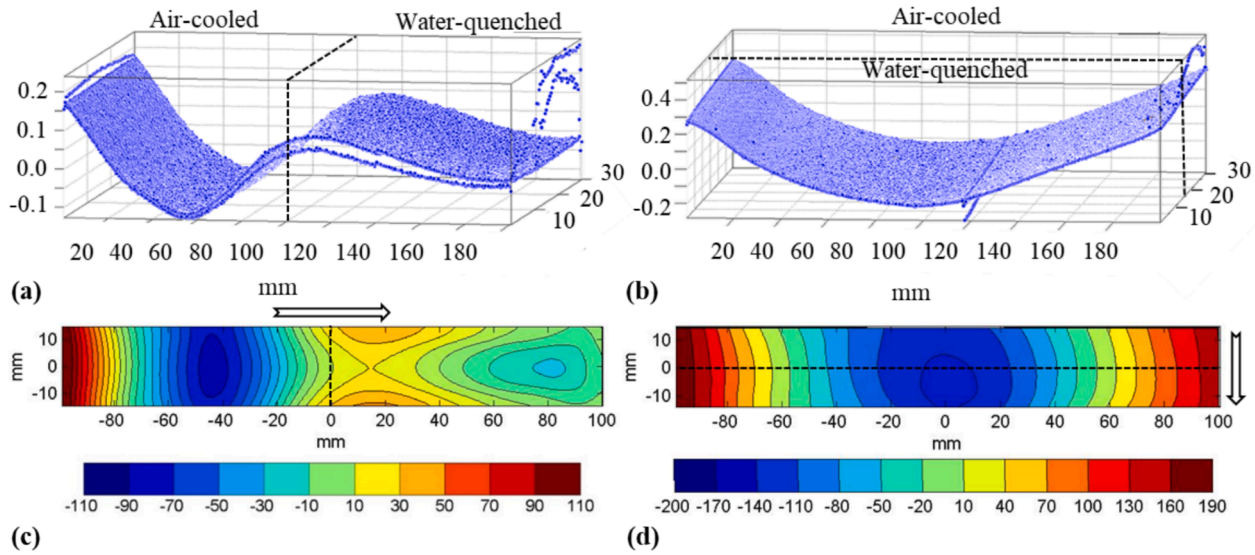

Fig. 7. (a) and (b) 3D point clouds measured by CMM on one half-side of each of the vertically and horizontally quenched plates, respectively, (c) and (d) their corresponding contour plots of averaged surface height. For each case the surface of both sides of the cuts were averaged using a knot spacing of 8.75 mm (i.e., optimised size) in both directions. The arrows show the direction of quenching, and the air-cooled and water-quenched sides are separated by a broken line.

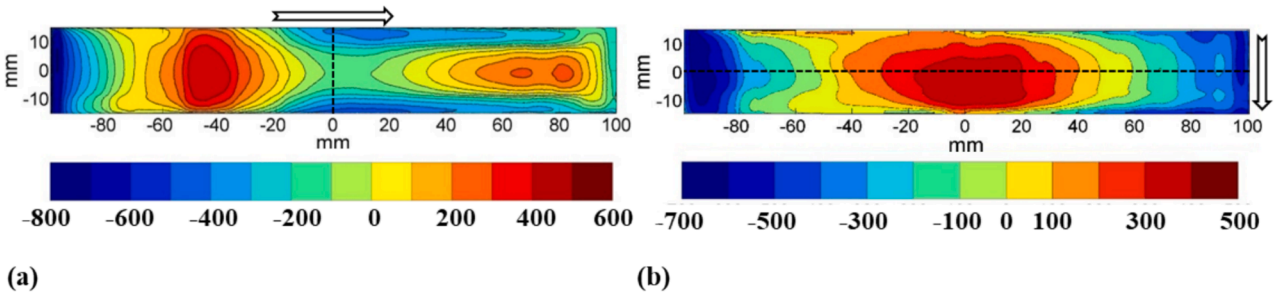

Fig. 8. (a) and (b) contour plots of the evaluated out-of-plane residual stress distributions following FE simulation using the averaged surface height (see Fig. 7) as boundary conditions for the vertically and horizontally quenched plates, respectively. The arrows show the direction of quenching, and the air-cooled and water-quenched sides are separated by a broken line.

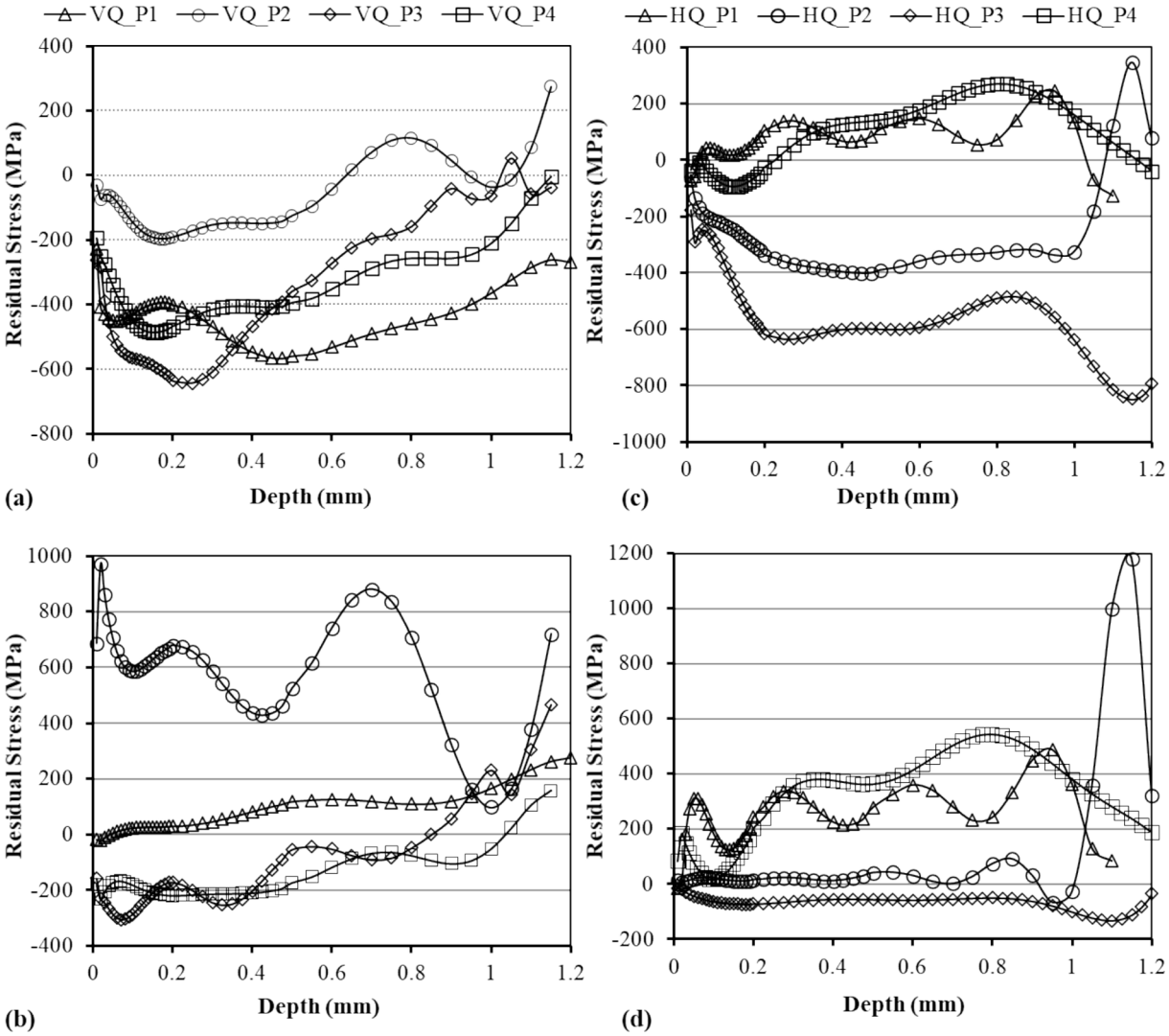

Fig. 9. Near surface residual stress profiles measured by ICHD on (a) and (b) the vertically quenched plate, (c) and (d) the horizontally quenched plate, along the length and along the width directions, respectively.

4. FE simulations

A series of FE simulations were carried out to predict the magnitudes and distributions of the residual stress, induced throughout the non-uniform quenching processes adapted in this study. The simulations included consecutive steps of (i) inverse analysis of HTC using the measured temperature profiles as boundary conditions, and (ii) implementation of the assessed HTCs in a thermal–mechanical FE model to simulate the quenching process and predict the associated residual stress.

4.1. Inverse analysis of HTC

The model implemented for the evaluation of HTCs, during both

water-quenching and air-cooling, uses the heat equation (Equation (1).

$$\rho C_p \frac{\partial T}{\partial t} = \lambda\left(\frac{\partial^2 T}{\partial x^2}+\frac{\partial^2 T}{\partial y^2}+\frac{\partial^2 T}{\partial z^2}\right)+\dot{q} \quad (1)$$

Where ρ, λ, C_p, and $\dot{q}$ are the material's density, thermal conductivity, heat capacity, and the internal thermal energy released due to microstructural changes (e.g., phase transformation), respectively. Although the internal thermal energy, $\dot{q}$, can be calculated as a function of the latent heat and the volume fraction of each phase in the microstructure (i.e., γ'' precipitate and the γ matrix), this has not been evaluated directly in this work. Instead, the overall heat flux has been evaluated by measuring the changes in thermal field using temperature check points at specified locations. The HTC has then been back-calculated using the measured cooling curves at specified locations as boundary conditions according to Equation (2).

$$\dot{Q} = hA(T_s - T_{env})$$

$$h = \frac{q}{\Delta T} \quad (2)$$

Where $\dot{Q}$ is the rate of heat transfer between the part and the environment, q is the heat flux per unit area ($q = \frac{d\dot{Q}}{dA}$) with $\frac{W}{m^2}$ dimension, h is the HTC with a unit of $\frac{W}{m^2.K}$, A is the surface area through which the heat transfer takes place, and T_s and T_{env} are respectively the temperature of the surface of the part and the surrounding environment. Note that the HTC includes both the convection and radiation in these analyses. Also, T_{env} for water-quenching and air-cooling were taken into consideration as the measured temperatures of the water and the laboratory, respectively.

A standard, iterative solution algorithm based on temperature gradients, distance from quenching faces and part geometry was applied through the commercial FE software DEFORM®. It has a dedicated module for calculating HTCs in either the temperature or time domain from a pre-selected number of control points. For each condition, a 3D model was constructed for inverse heat transfer analysis by considering a quarter of the whole geometry, taking benefit of implementing symmetry planes for simplification (i.e., and reduced computation time). Different symmetry planes were considered depending on the quenching

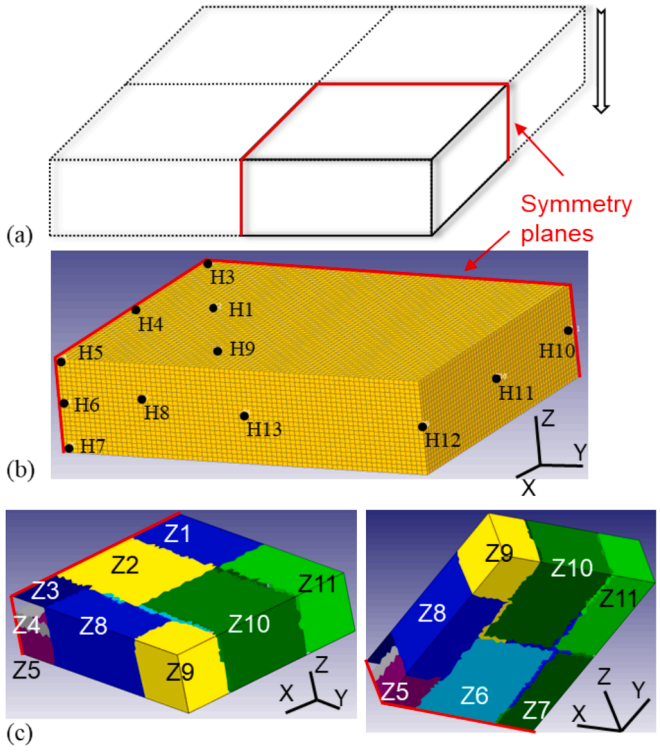

Fig. 11. Visualisation of the FE simulation setup for inverse calculation of HTCs in DEFORM® for the horizontally quenched/air-cooled plate; (a) a schematic sketch of the plate highlighting the symmetry planes and a quarter of the part considered for the simulation, (b) a CAD model of a quarter of the plate with assigned elements (i.e., meshed), highlighting the locations of the thermocouples, and (c) the same model as that in (b) with different zones considered for HTC calculation in which a zone has been assigned per thermocouple as a control point. In (c), images both top (left) and bottom (right) sides of the model are provided to show the assigned zones. Note that the locations of the thermocouples in (b) are matching those in the full plate shown schematically in Fig. 5d. The arrow shows the direction of water-quenching.

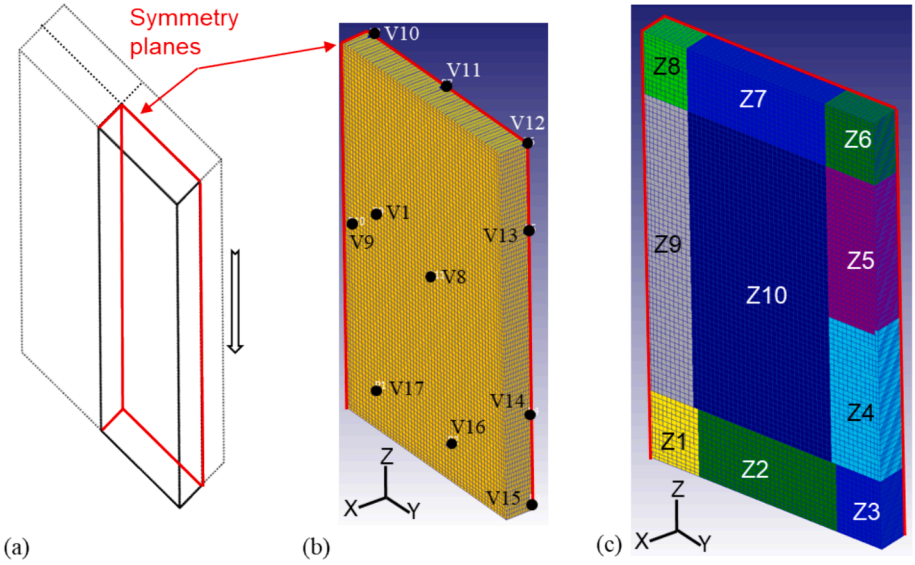

Fig. 10. Visualisation of the FE simulation setup for inverse calculation of HTCs in DEFORM® for the vertically quenched/air-cooled plate; (a) a schematic sketch of the plate highlighting the symmetry planes and a quarter of the part considered for the simulation, (b) a CAD model of a quarter of the plate with assigned elements (i.e., meshed), highlighting the locations of the thermocouples, and (c) the same model as that in (b) with different zones considered for HTC calculation in which a zone has been assigned per thermocouple as a control point. Note that the locations of the thermocouples in (b) are matching those in the full plate shown schematically in Fig. 4d. The arrow shows the direction of water-quenching.

configuration, as highlighted for both cases in Fig. 10a and Fig. 11a, respectively for the vertical and horizontal water-quenching/air-cooling. Initially, a coarse mesh with ~ 5 mm brick element was assigned to the interior and 3 layers of fine structured surface mesh with ~ 0.2 mm element of the same type to the periphery of the model. Fine surface elements determine and control the fast heat transfer with the environment and rough bulk elements determine the heat capacity and conductivity within the part. For enhancing the accuracy of the inverse heat transfer analysis, the positions of the thermocouples for temperature measurements were located very close to the finer mesh zones near the surface of the part. The selected element type and rough mesh size for the initial model were verified using reference HTCs. The selection of rough elements in the initial model was to reduce computational time and to interpolate computational errors within a short period of time.

Following the verification of the simulation setup in the initial model, each inverse HTC analysis for water-quenching was split into shorter time sections according to the temperature profiles recorded for areas with greater sensitivity to temperature changes (i.e., typically the corners). These sections included (i) the time period prior to the opening of the furnace door when all thermocouples were showing a uniform heat-treatment temperature (i.e., 980 °C), (ii) from the time when the furnace door was opened until the part has touched the water, including the transfer time, (iii) the film boiling stage (i.e., few seconds just after the part is immersed in water), (iv) transition and nucleate boiling stages, and (v) the final stage of quenching where the temperature of the part approaches the water temperature (i.e., from ~ 300 °C to the room temperature). These are shown for the vertical quenching in Fig. 4a and b. The inverse HTC analysis of the air-cooling trials was conducted in one single step, considering the entire cooling profile. The temperature dependant thermal properties of IN718 superalloy used in these simulations are provided in Table 2.

Breaking down the inverse HTC simulation for water-quenching was to assist the algorithm to converge towards the control points (i.e., the measured cooling curves) with ease within each stage and solve for the remaining temperature profile. The problem was solved in the time domain due to its flexibility and the availability of more control points. In these analyses, the periphery of the model was divided into zones (see Fig. 10b, c and Fig. 11b, c) where at least a zone, including the exterior elements, was assigned to each thermocouple for maximum flexibility. The applied methodology aimed to achieve a high level of convergence, with a fit of ± 5 °C at every point in time. The resulted HTCs describe the overall heat transfer between each zone of the part and the surrounding environment including radiation. Fig. 12 show the evaluated HTC profiles for all the considered zones of both vertical and horizontal configurations (see Fig. 10 and Fig. 11f or the zone numbers) for water-quenching and air cooling trials.

4.2. Residual stress prediction

The prediction of residual stress during non-uniform quenching (i.e., half in air and half in water) of the plates, in both vertical and horizontal quenching configurations, were carried out using 3D thermal–mechanical models in ABAQUS. For this purpose, the model was meshed using C3D20R element type with average size of 0.5 mm in the centre and finer 0.1 mm close to the periphery. The solution annealing heat treatment temperature (i.e., 980 °C) was assigned to the part as an initial temperature. To replicate the experimental quenching conditions, for both vertical and horizontal quenching configurations, the model was sectioned into two sides, one to simulate the exposure to water and the other to air. The evaluated HTCs, using inverse analysis method, for different zones during water-quenching and air-cooling were applied to the relevant surfaces as boundary conditions to simulate the evolution of temperature throughout the plates and heat flux out of the parts during non-uniform quenching. These HTC's determine the magnitude of heat exchange with the environments which relates the surface temperature of the part with heat flux [48]. The temperature dependant thermal-physical and thermal–mechanical properties of the material, presented in Table 2 were adopted. The variation in these properties as a function of alloy composition and heat treatment is negligible (i.e., <10 %).

Owing to the importance of the constitutive model for material's hardening behaviour and also the yield strength in the accuracy of residual stress prediction, a special setup was considered in the FE simulation. In agreement with a previous study [49], a rate-independent isotropic linear hardening model was implemented, considering a hardening coefficient of $d\sigma_y/d\varepsilon_p = 0.01E$. Since the material's yield strength changes with temperature, the yield data reported in a previous work [46] for solution treated IN718 were fitted to Equation (3) to obtain the evolution of yield strength as a function of temperature as provided in Table 2. This approach has successfully been implemented in a previous study [17] on the prediction of quenching induced residual stress in a small cylindrical specimen made from the same material. The material data used in the FE model (i.e., Table 2) were partially collected from the same batch of material as those used in this study, reported elsewhere [11], and from other reports in literature [46] that were all in a very good agreement.

$$\sigma_y(T) = \frac{\sigma_y^{RT} - \sigma_y^{HT}}{1 + \exp((T-b)/c)} \tag{3}$$

Where in Equation (3), σ_y^{RT} and σ_y^{HT} are the material yield strengths at the room temperature and at solution annealing temperature (i.e., above γ'' solvi), b and c are the constants evaluated from the best fit to the yield strengths curve (i.e., for the in Table 2). Note that the effects that the precipitation and dissolution of the strengthening phases (i.e., γ' and γ'') have on the yield strength of the superalloy [50] have been neglected in these analyses. Fig. 13a and b show the predicted out-of-plane (i.e., S33) residual stress distributions obtained by these FE simulations, respectively for the vertically and horizontally quenched plates.

Table 2
Thermo-physical and thermo-mechanical properties of IN718 material taken from [11,17,46,47], implemented in the FE analyses in this study.

Temperature (°C)	Thermal Conductivity (W m^{-1} K^{-1})	Density (kg m^{-3})	Specific Heat Capacity (J kg^{-1} K^{-1})	Mean Thermal Expansion Coefficient (×10^{-6})	Young's Modulus (GPa)	Yield Strength (MPa)
0	11.02	8226	424	12.8	197	300
100	12.75	8190	434	13.1	197	300
200	14.36	8160	448	13.4	197	300
300	15.96	8130	463	13.8	197	300
400	17.600	8090	480	14.2	197	300
500	19.18	8050	500	14.0.0	196	298
600	20.77	8010	525	15.1	194	295
700	22.36	7960	560	15.7	187	283
800	23.95	7910	605	16.4	165	248
850	24.53	7890	625	16.8	145	215
900	25.100	7860	636	17.1	130	173
1000	26.83	7810	645	17.5	105	94

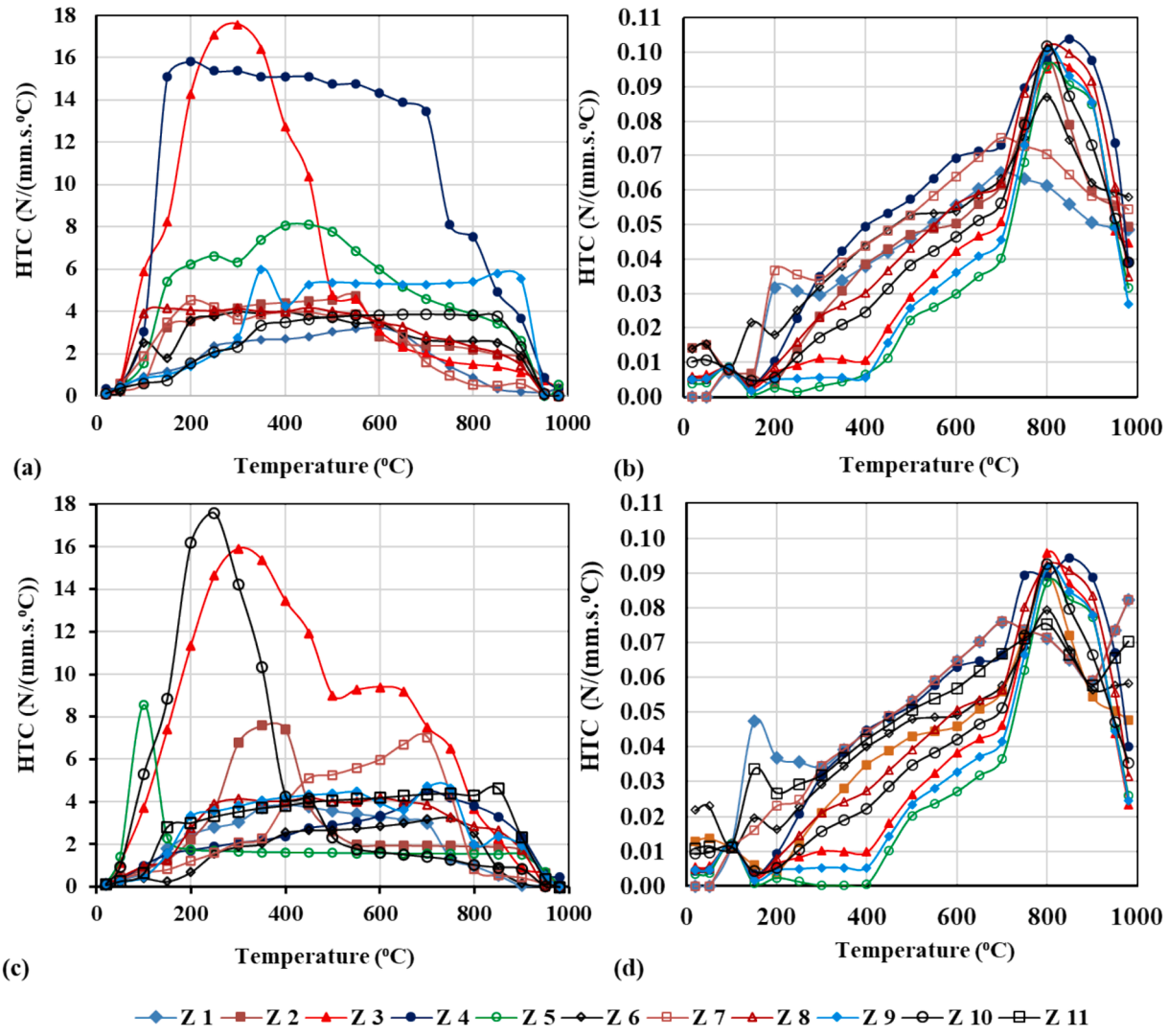

Fig. 12. The calculated HTC values as a function of temperature, using inverse heat transfer analysis method, for (a) vertical water-quenching, (b) vertical air-cooling, (c) horizontal water-quenching, and (d) horizontal air-cooling. See Fig. 10 and Fig. 11 for the position of each zone and the associated thermocouple.

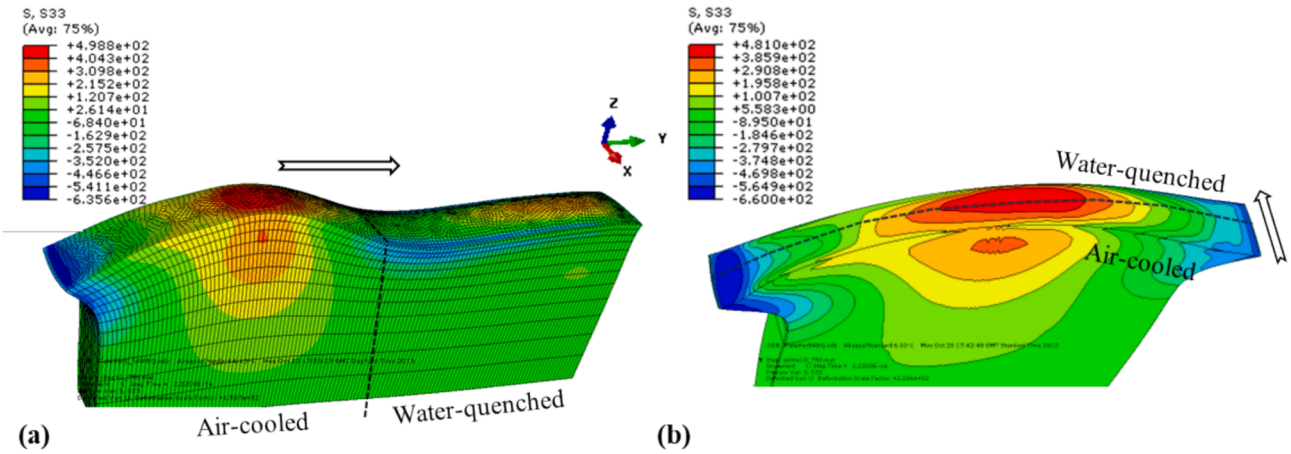

Fig. 13. The predicted out-of-plane residual stress distributions for the heterogeneously quenched plates (i.e., half in water and half in air); (a) vertical, and (b) horizontal configurations.

5. Discussion

Digitally representing the manufacturing processes and their associated changes in residual stress state can be achieved by simulation models, which can then be utilised for decision making on the selection and application of optimised process parameters. For this purpose, a

baseline model simulating the metal forging and heat treatment processes (i.e., hot working, aging, quenching) taking into consideration microstructural changes (e.g., phase transform, precipitations, grain growth) using physically based and constitutive materials models, can be developed [51,52]. However, with the current state-of-the-art simulation methodologies (software) and available hardware, forecasting the results of every stage in the production process at industrial scale cannot be achieved rapidly and accurately enough for in-process decision making. This is even more complicated when the manufacturing processes include quenching, giving rise to multi-physics and multi-scales simulations involving fluid flows which need numerical analysis methods for computational fluid dynamics (CFD) on top of materials thermo-mechanical and thermo-physical properties [53–55].

The methodology presented in this paper is a practical approach to simulate the magnitude and distribution of thermally induced residual stress during quenching processes. Using FE for inverse analysis of HTC based on material's thermo-physical properties and cooling curves, measured by embedding thermo-couples as close as possible to the exposed surfaces, eliminated the need for physically based CFD models. This approach allowed the calculation of HTCs for all the defined surfaces (i.e., averaged over each zone) (see Fig. 10 and Fig. 11), which were then used to predict the associated residual stress by implementing them into an elastic–plastic FE model. The predicted residual stress based on these HTC's were verified by measuring residual stress on the samples experimentally (see Fig. 14 and Fig. 15). A reasonably good agreement was obtained between the predicted and measured residual stress distributions for each case, as shown in Fig. 14a and Fig. 15a, implying the suitability of this approach (i.e., the use of invers HTC analysis) for the prediction of quenching induced residual stress during manufacturing.

Fig. 14b and Fig. 15b show comparisons between the predicted and measured out-of-plane residual stress profiles along a line of interest (i.e., C-C') in both the vertically and horizontally quenched plates, respectively. The overall predicted and measured stress profiles are reasonably close, emphasising that this methodology can simulate bulk residual stress for both quenching configurations reasonably well. Meanwhile, a discrepancy can be seen at local level between the predicted and measured residual stress profiles such that the results of the FE simulation appear to be smoother (i.e., local peaks and troughs have not been calculated). The discrepancy is more pronounced near the surfaces of the parts as shown at points P1 – P4 in Fig. 14c, d, e and f for the vertically quenched and at points P1, P2 and P4 in Fig. 15c, d and e for the horizontally quenched plates. The spatial resolution of the data measured by the contour method is a combination of several different parameters, including (i) the measurement pitch (i.e., 0.5 mm in this this case) implemented during the acquisition of the surface displacement profiles by the CMM, (ii) the smoothening effect of the applied surface fitting algorithm (i.e., cubic spline fitting), and (iii) the node density (i.e., element size) of the FE mesh used for the FE modelling. It is difficult to ascribe a quantitative value against these factors, but the results certainly have no greater spatial accuracy than the lowest resolution used in any of them. Therefore, the near surface residual stress measured by the contour method is affected the most by these factors, and hence the reason for the confirmatory measurements by the ICHD technique. Despite the significant uncertainty of the ICHD technique within the initial 0.5 mm distance from the surface, owing to the material removal and damages introduced by surface preparation for strain gauge rosette installation [56], the results are close to those of the contour method and the FE prediction. However, although measuring Type I macro residual stress, the ICHD measures stress at lower scales (i.e., compared to the contour method) and as a result more detailed stress profiles are obtained, which includes higher local stress data compared to the smoother profile obtained by the contour method.

As previously described, the contour method [36] is based on Bueckner's superposition principle, which relies on an elastic stress relaxation response following cutting using EDM (i.e., a relatively non-destructive and non-contact technique), allowing for the reverse calculation of residual stress using the 2D distribution of the out-of-plane surface displacements. As such, the accuracy and robustness of the results of residual stress determination by this method depends chiefly on the accuracy of the cutting process, the quality of the half-cut surfaces, and the points density of the acquired surface displacement data. To minimise inaccuracies associated with cutting and to eliminate potential part movement during the EDM cutting process, both plates investigated in this study were self-clamped by drilling two pilot holes at both ends of the cutting trajectory for the contour method and therefore leaving a ligament behind. This self-clamping method has been proven to be effective through previous measurements on far larger samples as reported in [39]. A comprehensive step-by-step procedure detailing good practice for different steps of residual stress measurement with the aid of contour method are provided in [57,58], including cutting, data processing, and numerical modelling, which were practiced in this work with additional tweaks from the authors (e.g., devising the pilot holes) based on previous experience. Following these procedures, a very clean dataset was obtained for the cut surfaces of both plates, with distinct continuous surface profiles for each of the quenching configuration and minimal evidence of interruption caused by artefacts, as shown in Fig. 7. For both vertical and horizontal quenching configurations (Fig. 7a, b) only a few outliers were observed at the edges, with the exception of the latter (Fig. 7b) where an outlier line was also present in the middle of both half-cuts, which was caused by a single wire breakage during the EDM cutting process. Once the accuracy of the cutting process and the quality of the half-cut surfaces were established, the data were then further processed by removing the outliers and through application of other steps as highlighted in the experimental procedure.

The codes used for these processes were developed in-house based on the methodology initially proposed and proven by Prime [36] and further developed into a platform by Johnson [59]. Other open-source packages, such as pyCM [60] and OxCM [61], exist which offer comprehensive data processing, numerical simulations and data analysis (post-processing), eliminating the need for separate libraries. The authors are well familiar with the pyCM solver and to the best of their knowledge, the step-by-step procedure followed in this study matches with those implemented in the pyCM platform. Meanwhile, although the contour method is a validated technique and multiple open-source packages exist [59–61] for its analyses, its accuracy heavily depends on the decisions made by the model user, especially if the data contains inaccuracies and artifacts that require significant cleaning and adjustments. Otherwise, the contour method is a well-established method of residual stress measurement that has been developed and verified using multiple alternative techniques on different materials and alloy systems, such as validation with neutron diffraction using welds [62–64] and railway tracks [65], and validation with XRD, ICHD and deep hole drilling using welded Ti-6Al-4V [38] and cladded Inconel 625 [39]. The Net Task Group 4 [66] studies also provide additional validations of the contour method using a wide range of experimental and numerical methods.

Water-quenching has resulted in severe heat exchange (i.e., large HTCs [25]) with the quenchant over the entire process, compared to air-cooling, until the time when the temperature falls below 100 °C at which point the convection takes over (see Fig. 12). In absence of any external agitation, the film boiling stage appeared to be dominated by the formation of a stable and persistent blanket of vapour covering the part, at least partially, during the initial phase of both quenching configurations (see V3, V4, V8 & V9 in Fig. 4b and H3, H4, H8 & H9 in Fig. 5b). This had resulted in a relatively limited heat transfer, as evidenced by the significantly slower cooling rate measured at the beginning of quenching shown in Fig. 4b and Fig. 5b, until the temperature falls below the Leidenfrost temperature below which the vapour blanket collapses, leading to the start of a very vigorous nucleate boiling stage. This is manifested in the high HTCs for zones Z3, Z4, Z5 and Z10 in the vertically and horizontally quenched plated, respectively (see Fig. 12).

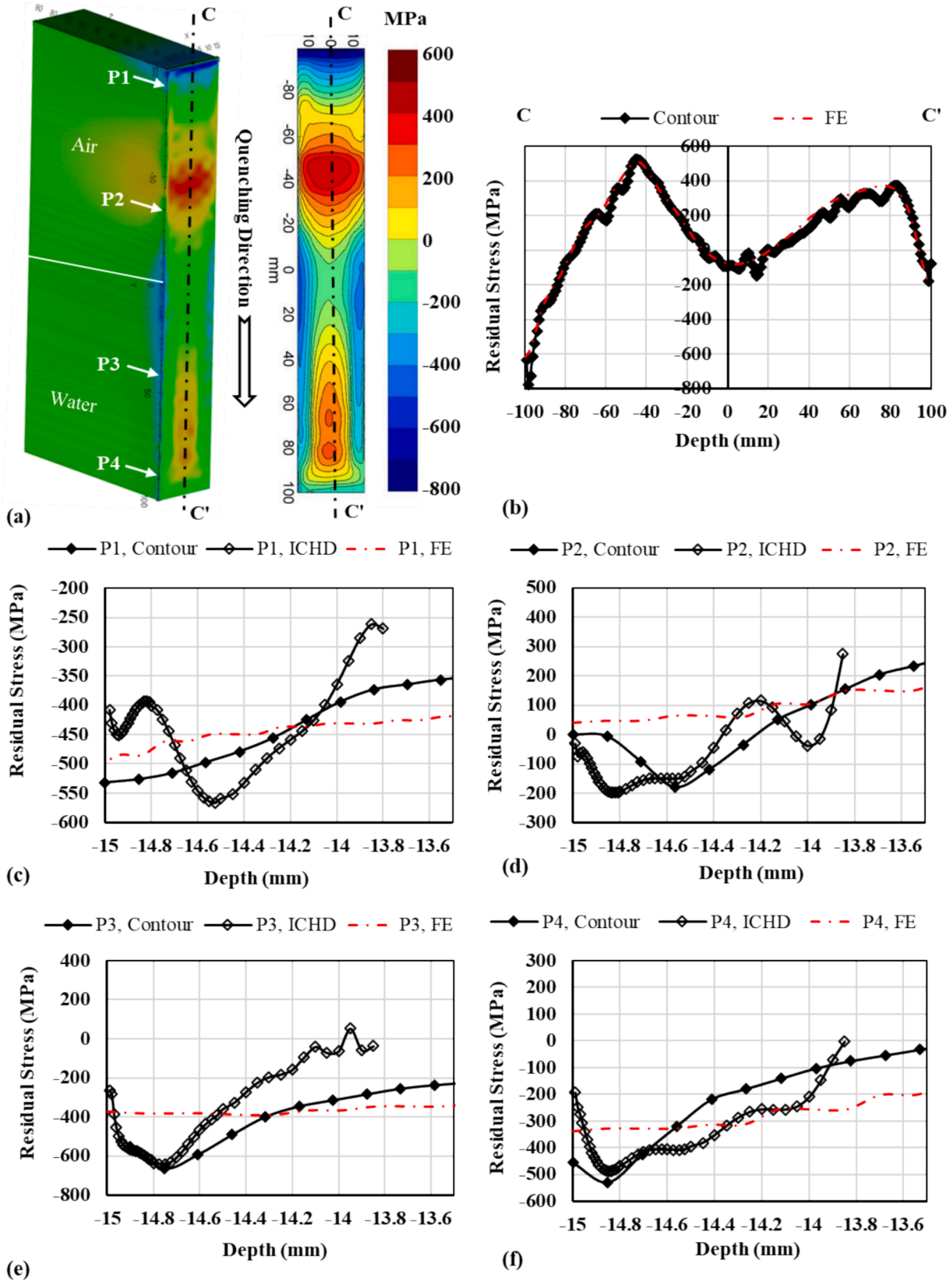

Fig. 14. Comparisons between the measured and predicted residual stress including (a) contour plots of out-of-plane residual stress distribution predicted by FE (left) and measured by the contour method (right), (b) residual stress profiles along the C-C' line highlighted in (a) for both the FE predicted and measured stress by contour method, (c), (d), (e) and (f) residual stress profiles in the proximity of the surface of the part at P1, P2, P3 and P4 locations, respectively, highlighted in (a). See Fig. 2 for the precise locations of the measurements points with ICHD.

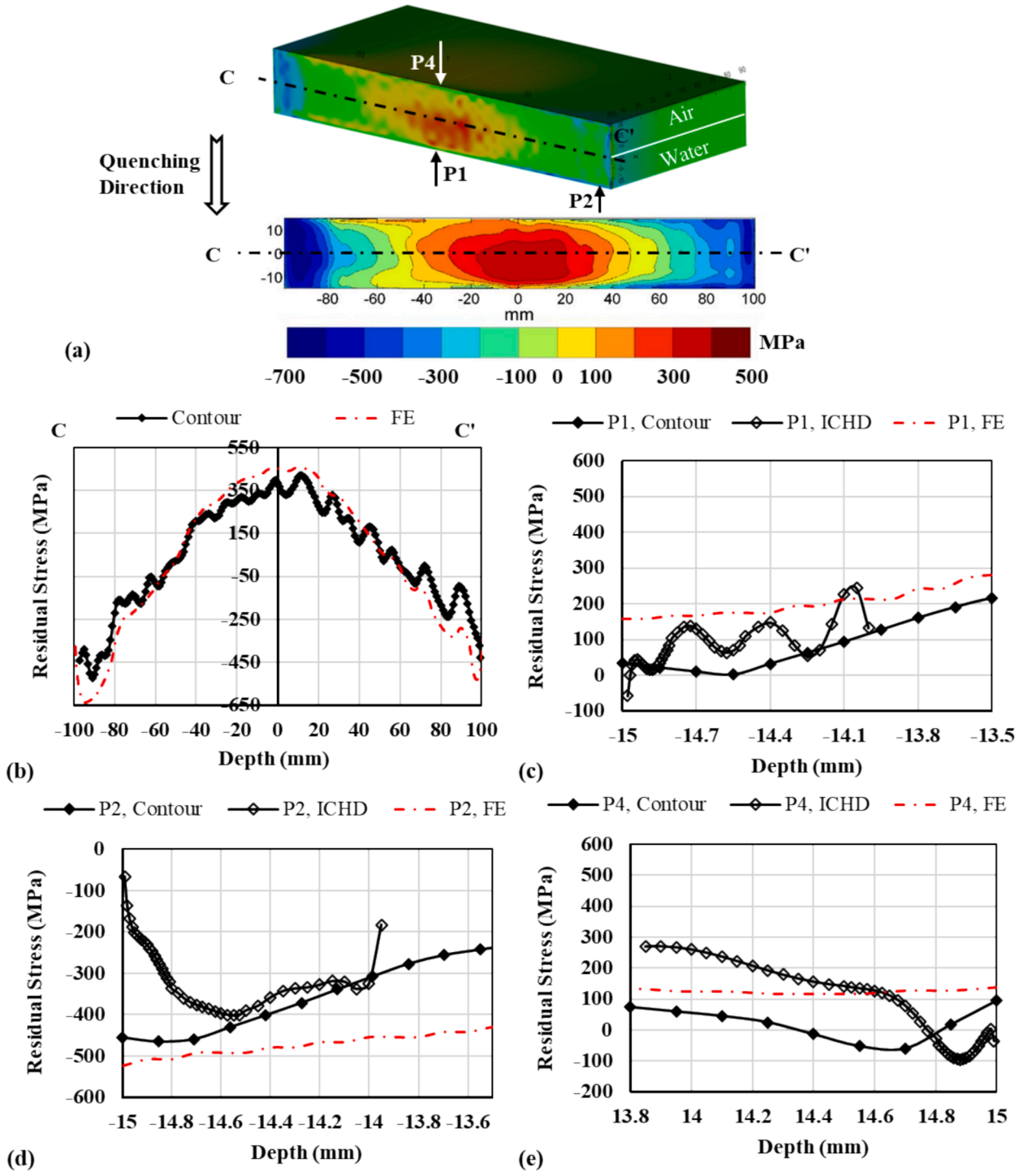

Fig. 15. Comparisons between the measured and predicted residual stress including (a) contour plots of out-of-plane residual stress distribution predicted by FE (top) and measured by the contour method (bottom), (b) residual stress profiles along the C-C' line highlighted in (a) for both the FE predicted and measured stress by contour method, (c), (d), and (e) residual stress profiles at the surface proximities at P1, P2, P3 and P4 locations, respectively, highlighted in (a). See Fig. 2 for the precise locations of the measurements points with ICHD.

Fig. 12 clearly demonstrates the significant difference between the calculated HTCs for various zones in both plates, implying the importance of sample configuration (and geometrical features for more complex parts) on the heat exchange rate. These differences in the cooling rates leads to the generation of residual stress due to heterogeneous plastic deformation at the surface, as reported also in previous works [67,68].

The observed differences in the cooling rates between different regions of a part, could potentially lead to heterogeneous precipitation in the material such that larger number of γ'' with smaller average size nucleate and grow in areas undergoing faster cooling rates, and smaller number of γ'' with larger average size in areas undergoing slower cooling rates [1]. This may change the material's elastic properties which may then affect the residual stress magnitude and distribution. This cannot be picked up by the measurement techniques (contour method and ICHD) used in this study due to the consideration of an

average Young's modules (i.e., uniform material) throughout the part.

In the existing state-of-the-art manufacturing methods, components are usually quenched/cooled individually or in batches without any control over the cooling rates of different regions of a part locally, resulting in undesirably distributed residual stress fields, with inconsistency from part to part (e.g., vertical vs. horizontal). These inconsistencies in the stress field result in random distortion out of dimensional tolerances when the same material removal strategy is used for their final machining. Even if machining is done successfully, the inconsistency in the stress distribution leads to huge uncertainties in life-expectancy prediction of a part, leading to consideration of large safety factors for life-in-service, i.e., the full potential of the material is not used. The ideal manufacturing method, which will inevitably be practiced in future, will be to apply varying cooling rates, in-process, to different regions of a part to generate residual stress field of desired magnitude and distribution. The desired cooling rates or temperature time histories can be obtained by modelling, where (i) the desired microstructure will be identified based on set targets and material behaviour, (ii) the desired residual stress field will be determined by the required stress distribution for optimised right-first-time machining operations and those beneficial to the performance, and (iii) an optimum solution will be applied by the most cost-effective and specification favourable scenario by balancing microstructure and residual stress.

6. Conclusion

In this study, the generation of residual stress in IN718 nickel-based superalloy plate during non-uniform cooling has been investigated. The major outcomes of this work are concluded as follows:

- A pragmatic methodology has been described and verified for the prediction of quenching induced residual stress during non-uniform quenching of IN718 nickel-based superalloy component that can be utilised for optimisation of industrial scale manufacturing processes. This was based on inverse calculation of heat transfer coefficient (HTC), which has then been used as boundary conditions for the prediction of residual stress generation and distribution.
- The described methodology, i.e., based on inverse HTC analysis, eliminates the need for more complex and time-consuming physically based CFD models which are often very difficult to define and implement for the simulation of large-scale components. The results predicted via this methodology have been verified by measuring residual stress experimentally using contour and hole-drilling methods.
- The magnitude and distributions of the predicted residual stress by FE simulation, based on HTCs, were in reasonable agreement with those measured by the contour method. Both the measured and simulated data in the plate geometry suggest that quenching configuration (i.e., vertically, or horizontally) plays a major role in determining the heat exchange rate (i.e., HTC) between different regions of the part and the quenchant (i.e., water), which in turn leads to completely different distributions of the resulting residual stress.
- Despite its destructiveness, the contour method of residual stress measurement provided excellent reading of the stress fields with enough sensitivity to capture the effect of quenching configuration on stress distribution.
- Finally, the methodology introduced in this study can be implemented by engineers for optimisation of manufacturing process of more complex real parts, such as turbine discs, to accurately estimate the magnitude and distribution of quenching induced residual stress and the effect of part's configuration during quenching. This can then be used to design machining strategy and materials removal tool path to achieve the final geometry within the required dimensional tolerances, i.e., promoting right-first-time manufacturing.

CRediT authorship contribution statement

S. Rahimi: Writing – review & editing, Writing – original draft, Visualization, Validation, Supervision, Software, Resources, Project administration, Methodology, Investigation, Funding acquisition, Formal analysis, Data curation, Conceptualization. **M. King:** Writing – review & editing, Validation, Project administration, Formal analysis, Data curation. **M.Amir Siddiq:** Writing – review & editing, Visualization, Validation, Supervision, Software, Methodology, Conceptualization. **B.P. Wynne:** Writing – review & editing, Supervision, Resources.

Declaration of competing interest

The authors declare the following financial interests/personal relationships which may be considered as potential competing interests: Salaheddin Rahimi reports financial support, article publishing charges, and equipment, drugs, or supplies were provided by University of Strathclyde. If there are other authors, they declare that they have no known competing financial interests or personal relationships that could have appeared to influence the work reported in this paper.

Acknowledgements

The works were carried out at the Advanced Forming Research Centre (AFRC), University of Strathclyde (United Kingdom (UK)), which receives partial financial support from the UK's High Value Manufacturing CATAPULT (HVMC).

Data availability

Data will be made available on request.

References

[1] J. W. Brooks, P. J. Bridges, Metallurgical stability of inconel Alloy 718, in: S. Reichman, D.N. Duhl, G. Maurer, S. Antolovich and C. Lund (Ed.) Superalloys 1988, The Metallurgical Society, 1988.
[2] M. Dehmas, J. Lacaze, N. Niang, B. Viguier, TEM Study of High-Temperature Precipitation of Delta Phase in Inconel 718 Alloy, Adv. Mater. Sci. Eng. 2011 (2011) 1–9.
[3] S. Azadian, L. Y. Wei, F. Niklasson, R. Warren, Precipitation in spray-formed IN 718, in: E.A. Loria (Ed.) Superalloys 718, 625 and various derivatives, Minerals, Metals & Materials Society, Warrendale, PA7, 2001.
[4] Y. Desvallées, M. Bouzidi, F. Bois, N. Beaude, Delta phase in Inconel 718: mechanical properties and forging process requirements, in: E.A. Loria (Ed.) Superalloy 718-metallurgy and applications, Minerals, Metals & Materials Society, Warrendale, PA7 1994, pp. 281- 291.
[5] G. Sjfberg, N.G. Ingesten, Grain boundary y-phase morphology, carbides and notch rupture sensitivities of cast alloy 718, in: E.A. Loria (Ed.), Superalloy 718-Metallurgy and Applications, Minerals, Metals & Materials Society, Warrendale, PA7, 1991, pp. 603–621.
[6] J.F. Muller, M.J. Donachie, Superalloys a technical guide, ASM international, Materials Park, OH7, 1975.
[7] A. Thomas, M. El-Wahabi, J.M. Cabrera, J.M. Prado, High temperature deformation of Inconel 718, J. Mater. Process. Technol. 177 (1) (2006) 469–472.
[8] A. Coyne-Grell, J. Blaizot, S. Rahimi, I. Violatos, S. Nouveau, C. Dumont, A. Nicolaÿ, N. Bozzolo, Recrystallization mechanisms and associated microstructure evolution during billet conversion of a gamma-gamma′ nickel based superalloy, J. Alloy. Compd. 916 (2022) 165465.
[9] A. Coyne-Grell, J. Blaizot, S. Rahimi, I. Violatos, S. Nouveau, C. Dumont, A. Nicolaÿ, N. Bozzolo, Evolution of γ′ Precipitation During the Early Stages of Industrial Forging of a Nickel-Based Superalloy, Metall. Mater. Trans. A 54 (5) (2023) 2022–2036.
[10] R.C. Reed, The Superalloys: Fundamentals and Applications, Cambridge University Press, 2006.
[11] S. Rahimi, M. King, C. Dumont, Stress relaxation behaviour in IN718 nickel based superalloy during ageing heat treatments, Mater. Sci. Eng. A 708 (2017) 563–573.
[12] C. Slama, M. Abdellaouib, Structural Characterization of the Aged Inconel 718, J. Alloys Compd. 306 (2000) 277–284.
[13] M. King, S. Rahimi, Optimisation of sample geometry for thermo-mechanical testing of precipitation hardenable nickel-based superalloys with an ETMT machine, Strain 60 (1) (2024) e12458.
[14] R.D. Lopez-Garcia, I. Medina-Juárez, A. Maldonado-Reyes, Effect of Quenching Parameters on Distortion Phenomena in AISI 4340 Steel, Metals 12 (5) (2022) 759.
[15] M.T. Todinov, Influence of some parameters on the residual stresses from quenching, Model Simul, Mater. Sci. Eng. 7 (1999) 25–41.

[16] Y. Nagasaka, J.K. Brimacombe, E.B. Hawbolt, I.V. Samarasekera, B. Hernandez-Morales, S.E. Chidiac, Mathematical model of phase transformations and elastoplastic stress in the water spray quenching of steel bars, Metall. Trans. A 24 (4) (1993) 795–808.
[17] D. Dye, K.T. Conlon, R.C. Reed, Characterization and modeling of quenching-induced residual stresses in the nickel-based superalloy IN718, Metall. Mater. Trans. A 35 (6) (2004) 1703–1713.
[18] P.J. Withers, H.K.D.H. Bhadeshia, Residual stress. Part 2 – Nature and origins, Mater. Sci. Technol. 17 (4) (2001) 366–375.
[19] M.I. Davidzon, Newton's law of cooling and its interpretation, Int. J. Heat Mass Transf. 55 (21) (2012) 5397–5402.
[20] R. Kamenicky, S. Rahimi, I. Violatos, K. Ritos, Numerical modelling of the Water-Quenching Process validated through experiments with IN718 Nickel-Based Superalloy, Int. J. Heat Mass Transf. 235 (2024) 126158.
[21] Y. Bouissa, D. Shahriari, H. Champliaud, M. Jahazi, Prediction of heat transfer coefficient during quenching of large size forged blocks using modeling and experimental validation, Case Stud. Therm. Eng. 13 (2019) 100379.
[22] X. Zhang, Y.E. Ma, W. Li, W. Huang, W. Zhang, Z. Wang, A review of residual stress effects on fatigue properties of friction stir welds, Crit. Rev. Solid State Mater. Sci. 48 (6) (2023) 775–813.
[23] G.H. Farrahi, J.L. Lebrijn, D. Couratin, Effect of shot peening on residual stress and fatigue life of a spring steel, Fatigue Fract. Eng. Mater. Struct. 18 (2) (1995) 211–220.
[24] S. Rahimi, K. Mehrez, T.J. Marrow, Effect of surface machining on intergranular stress corrosion cracking (IGSCC) in sensitised type 304 austenitic stainless steel, Corros. Eng. Sci. Technol. 51 (5) (2016) 383–391.
[25] H. Hu, C. Xu, Y. Zhao, K.J. Ziegler, J.N. Chung, Boiling and quenching heat transfer advancement by nanoscale surface modification, Sci. Rep. 7 (1) (2017) 6117.
[26] H.K. Kim, S.I. Oh, Evaluation of heat transfer coefficient during heat treatment by inverse analysis, J. Mater. Process. Technol. 112 (2) (2001) 157–165.
[27] L. Huiping, Z. Guoqun, N. Shanting, L. Yiguo, Inverse heat conduction analysis of quenching process using finite-element and optimization method, Finite Elem. Anal. Des. 42 (2006) 1087–1096.
[28] H. Li, G. Zhao, L. He, Y. Mu, High-speed data acquisition of the cooling curves and evaluation of heat transfer coefficient in quenching process, Measurement 41 (6) (2008) 676–686.
[29] S. Chantasiriwan, Inverse determination of steady-state heat transfer coefficient, Int. Commun. Heat Mass Transf. 27 (8) (2000) 1155–1164.
[30] A. Sugianto, M. Narazaki, M. Kogawara, A. Shirayori, A comparative study on determination method of heat transfer coefficient using inverse heat transfer and iterative modification, J. Mater. Process. Technol. 209 (10) (2009) 4627–4632.
[31] B. Xiao, Q. Wang, P. Jadhav, K. Li, An experimental study of heat transfer in aluminum castings during water quenching, J. Mater. Process. Technol. 210 (14) (2010) 2023–2028.
[32] D. Dye, B.A. Roder, S. Tin, M.A. Rist, J.A. James, M.R. Daymond, Modeling and Measurement of Residual Stresses in a Forged IN718 Superalloy Disc, Superalloys 2004 (2004) 315–322.
[33] M.A. Rist, S. Tin, B.A. Roder, J.A. James, M.R. Daymond, Residual stresses in a quenched superalloy turbine disc: Measurements and modeling, Metall. Mater. Trans. A Phys. Metall. Mater. Sci. 37 (2) (2006) 459–467.
[34] Y. Dahan, S. Nouveau, E. Georges, B. Flageolet, Residual stresses in Inconel 718 engine disks, MATEC Web Conf. (2014) 10003.
[35] ASTM International, Standard Test Method for Determining Residual Stresses by the Hole-Drilling Strain-Gage Method, E837–13a, ASTM International, West Conshohocken, PA, USA, 2013.
[36] M.B. Prime, Cross-Sectional Mapping of Residual Stresses by Measuring the Surface Contour After a Cut, J. Eng. Mater. Technol. 123 (2) (2001) 162–168.
[37] M. Prime, R. Sebring, J. Edwards, J. Baumann, R. Lederich, Contour method determination of parent part residual stresses using a partially relaxed FSW test specimen, SEM X Int. Congress and Exposition on Experimental and Applied Mechanics, Costa Mesa, CA, USA, 2004.
[38] W. Rae, Z. Lomas, M. Jackson, S. Rahimi, Measurements of residual stress and microstructural evolution in electron beam welded Ti-6Al-4V using multiple techniques, Mater Charact 132 (2017) 10–19.
[39] G. Benghalia, S. Rahimi, J. Wood, H. Coules, S. Paddea, Multiscale Measurements of Residual Stress in a Low-Alloy Carbon Steel Weld Clad with IN625 Superalloy, Mater. Perform. Charact. 7 (4) (2018) 606–629.
[40] J. Pollard, S. Rahimi, A. Watford, M. Jackson, B. Wynne, The Determination of Residual Stress in Extruded Ti-6Al-4V by Contour Method and Finite Element Analysis, Proceedings of the 13th World Conference on Titanium, Wiley Online Library, 2016, pp. 305-310.
[41] M.B. Prime, A.T. DeWald, The contour method, in: G.S. Schajer (Ed.) Practical residual stress measurement methods, Wiley 2013, pp. 109-138.
[42] P. Pagliaro, M.B. Prime, H. Swenson, B. Zuccarello, Measuring Multiple Residual-Stress Components using the Contour Method and Multiple Cuts, Exp. Mech. 50 (2) (2010) 187–194.
[43] M. Sundararaman, P. Mukhopadhyay, S. Banerjee, Precipitation of the δ-Ni3Nb phase in two nickel base superalloys, Metall. Trans. A 19 (3) (1988) 453–465.
[44] Y. Desvallées, M. Bouzidi, F. Bois, N. Beaude, Superalloys 718 and Derivatives, in: E.A. Loria (Ed.) TMS, 1994, pp. 281-291.
[45] B. Sobac, A. Rednikov, S. Dorbolo, P. Colinet, Chapter 7 - Leidenfrost Drops, in: D. Brutin (Ed.), Droplet Wetting and Evaporation, Academic Press, Oxford, 2015, pp. 85–99.
[46] H. Temperature, High Strength Nickel-Base Alloys, Nickel Development Institute, London, 1995.
[47] A.H. Committee, Properties and Selection: Irons, Steels, and High-Performance Alloys, ASM, International (1990).
[48] R.I. Ramakrishnan, T.E. Howson, Modeling the heat treatment of superalloys, JOM 44 (1992) 29–32.
[49] J. Goldak, M. Bibby, J. Moore, R. House, B. Patel, Computer modeling of heat flow in welds, Metall. Trans. B 17 (1986) 587–600.
[50] M.P. Jackson, R.C. Reed, Heat treatment of UDIMET 720Li: the effect of microstructure on properties, Mater. Sci. Eng. A 259 (1) (1999) 85–97.
[51] F. Han, F. Roters, D. Raabe, Microstructure-based multiscale modeling of large strain plastic deformation by coupling a full-field crystal plasticity-spectral solver with an implicit finite element solver, Int. J. Plast 125 (2020) 97–117.
[52] F. Roters, P. Eisenlohr, L. Hantcherli, D.D. Tjahjanto, T.R. Bieler, D. Raabe, Overview of constitutive laws, kinematics, homogenization and multiscale methods in crystal plasticity finite-element modeling: Theory, experiments, applications, Acta Mater. 58 (4) (2010) 1152–1211.
[53] G. El Haber, J. Viquerat, A. Larcher, D. Ryckelynck, J. Alves, A. Patil, E. Hachem, Deep learning model to assist multiphysics conjugate problems, Phys. Fluids 34 (1) (2022).
[54] E. Hachem, G. Jannoun, J. Veysset, M. Henri, R. Pierrot, I. Poitrault, E. Massoni, T. Coupez, Modeling of heat transfer and turbulent flows inside industrial furnaces, Simul. Model. Pract. Theory 30 (2013) 35–53.
[55] E. Hachem, T. Kloczko, H. Digonnet, T. Coupez, Stabilized finite element solution to handle complex heat and fluid flows in industrial furnaces using the immersed volume method, Int. J. Numer. Meth. Fluids 68 (1) (2012) 99–121.
[56] S. Rahimi, I. Violatos, Comparison Between Surface and Near-Surface Residual Stress Measurement Techniques Using a Standard Four-Point-Bend Specimen, Exp. Mech. 62 (2) (2022) 223–236.
[57] Erratum: 'Towards good practice guidelines for the contour method of residual stress measurement', The Journal of Engineering 2015(3) (2015) 92-92.
[58] F. Hosseinzadeh, J. Kowal, P.J. Bouchard, Towards good practice guidelines for the contour method of residual stress measurement, The Journal of Engineering 2014 (8) (2014) 453–468.
[59] G. Johnson, Residual stress measurements using contour method, The University of Manchester, Manchester, UK, School of Materials, 2008.
[60] M.J. Roy, N. Stoyanov, R.J. Moat, P.J. Withers, pyCM: An open-source computational framework for residual stress analysis employing the Contour Method, SoftwareX 11 (2020) 100458.
[61] F. Uzun, A.M. Korsunsky, The OxCM contour method solver for residual stress evaluation, Eng. Comput. 40 (5) (2024) 3059–3072.
[62] P.J. Bouchard, The NeT bead-on-plate benchmark for weld residual stress simulation, Int. J. Press. Vessel. Pip. 86 (1) (2009) 31–42.
[63] M. Kartal, M. Turski, G. Johnson, M.E. Fitzpatrick, S. Gungor, P.J. Withers, L. Edwards, Residual Stress Measurements in Single and Multi-Pass Groove Weld Specimens Using Neutron Diffraction and the Contour Method, Mater. Sci. Forum 524–525 (2006) 671–676.
[64] Y. Zhang, S. Ganguly, V. Stelmukh, M.E. Fitzpatrick, L. Edwards, Validation of the Contour Method of Residual Stress Measurement in a MIG 2024 Weld by Neutron and Synchrotron X-ray Diffraction, Journal of Neutron Research 11 (2003) 181-185.
[65] J. Kelleher, M.B. Prime, D. Buttle, P.M. Mummery, P.J. Webster, J. Shackleton, P. J. Withers, The Measurement of Residual Stress in Railway Rails by Diffraction and other Methods, J. Neutron Res. 11 (2003) 187–193.
[66] M.C. Smith, A.C. Smith, C. Ohms, R.C. Wimpory, The NeT Task Group 4 residual stress measurement and analysis round robin on a three-pass slot-welded plate specimen, Int. J. Press. Vessel. Pip. 164 (2018) 3–21.
[67] J.A. Nicol, E.D. Seaton, G.W. Kuhlman, H. Yu, R. Pishko, New quenchant for aluminum, Adv. Mater. Process. 149 (4) (1996) S40.
[68] J.S. Robinson, D.A. Tanner, S. van Petegem, A. Evans, Influence of quenching and aging on residual stress in Al–Zn–Mg–Cu alloy 7449, Mater. Sci. Technol. 28 (4) (2012) 420–430.